Novel Green Light Emitting Diodes: Exploring Droop-free Lighting Solutions for a Sustainable Earth

M. Razeghi*, C. Bayram and R. McClintock, F. Hosseini Teherani, D.J. Rogers and V. E. Sandana

Abstract— **The total annual energy consumption in the United States for lighting is approximately 800 Terawatt-hours and costs $80 billion to the public. The energy consumed for lighting throughout the world entails to greenhouse gas emission equivalent to 70% of the emissions from all the cars in the world. Novel solutions to lighting with higher efficiency will drastically reduce the energy consumption and help greenhouse gas emissions to be lowered. Novel green light emitting diodes are the key components of an affordable, durable and environmentally benign lighting solution that can achieve unique spectral quality and promise superior energy conversion efficiency.**

Light-emitting diodes (LEDs), based on the InGaN alloy, are currently the most promising candidates for realizing solid state lighting (SSL). InGaN is a direct wide bandgap semiconductor with an emission that can span the entire visible spectrum via compositional tuning. However, InGaN LED performance remains wavelength-dependent. Indeed, ultrabright and efficient blue InGaN-based LEDs are readily available but the performance of InGaN-based green LEDs is still far from adequate for use in SSL.

Our recent work demonstrated hybrid green light-emitting diodes (LEDs) comprised of n-ZnO/(InGaN/GaN) multi-quantum-wells/p-GaN were grown on semi-insulating AlN/sapphire using pulsed laser deposition for the n-ZnO and metal organic chemical vapor deposition for the other layers.. We have shown that atop grown ZnO layer by Pulsed Laser Deposition can be a good replacement for GaN. The green wavelength emission requires significant indium content in the active layer (growth temperature ~ 700ºC) that makes InGaN quantum wells very susceptible to thermal degradation. With our technology, diffusion and segregation of indium in the green emitting active is inhibited thanks to the lower ZnO deposition temperatures (<600ºC) than is required for GaN (>1000ºC). Our novel technology preserves the integrity of the as-grown active layer and demonstrates superior green spectral quality (as demonstrated for LEDs on *c*-sapphire). The results indicate that hybrid LED structures could hold prospects for the development of green LEDs with superior performance.

Index Terms— **green light-emitting diode, InGaN/GaN multi-quantum wells, InGaN quantum dots, metalorganic chemical vapor deposition, pulsed laser deposition, ZnO**

Manuscript received February 5, 2010.

M. Razeghi, C. Bayram and R. McClintock are with the Center for Quantum Devices, EECS Dept., Northwestern University. M. Razeghi contact details: (phone 1 (847) 491-7251; fax 1 (847) 476-1817; razeghi@eecs.northwestern.edu; http://cqd.eecs.northwestern.edu)

F. Hosseini Teherani, D. J. Rogers and V. E. Sandana are with Nanovation, 103b rue de Versailles, Orsay, France.

I. INTRODUCTION

III-Nitride based emitters support promising applications from water purification to solid state lighting due to their tunable direct bandgap extending from deep ultraviolet towards green.

In section 2 “Ultraviolet Light Emitting Diodes”, we are summarizing the research on ultraviolet light emitting diodes (LEDs). In section 3 “Hybrid Ultraviolet Light Emitting Diodes” we investigate some new ultraviolet LEDs based on silicon, zinc oxide and gallium nitride hybridization.

In section 4 “Comprehensive study of blue and green multi-quantum-well light emitting diodes grown on conventional and lateral epitaxial overgrowth GaN”, growths of blue and green multi-quantum-wells (MQWs) and light-emitting diodes (LEDs) are realized on lateral epitaxial overgrowth (LEO) GaN, and compared with identical structures grown on conventional GaN. Atomic force microscopy is used to confirm the significant reduction of dislocations in the wing region of our LEO samples before active region growth. Differences between surface morphologies of blue and green MQWs are analyzed. These MQWs are integrated into LEDs. All devices show a blue shift in electroluminescence (EL) peak, and narrowing in EL spectra with increasing injection current, both characteristics attributed to the bandgap renormalization. Green LEDs show a larger EL peak shift and broader EL spectrum due to larger piezoelectric field and more indium segregation in the MQWs, respectively. Blue LEDs on LEO GaN show a higher performance than those on conventional GaN, however, no performance difference is observed for green LEDs on LEO GaN versus conventional GaN. The performance of the green LEDs is shown to be primarily limited by the active layer growth quality.

Increasing the In content of the active layer, an apparent decrease in the intensity is observed. In section 5 “Green Light Emitting Diodes”, we identify the problem, and apply our unique pulsed epitaxy approach to achieve green LEDs.

In section 6 “Novel Hybrid Green LEDs Based on Substituting n-type ZnO for *n*-type GaN in an Inverted p-n Junction”, we demonstrate our unique approach for green light emitting diodes. Although ultra-bright and efficient blue InGaN-based Light Emitting Diodes (LEDs) are readily available, the performance of InGaN-based green LEDs is still relatively poor. This is because the higher In content required

in the active layers for green emission causes problems. In particular, the elevated substrate temperature (Ts) necessary for the *p*-type GaN top layer causes In to leak out of the active layers in the InGaN/GaN Multi-Quantum Wells (MQW). This significantly reduces the performance and lifetime of the LEDs. In this work, an *n*-type ZnO was substituted for the *n*-type GaN layer in an (In)GaN-based green LED with an inverted *p-n* structure. The top layer was thus the *n*-type ZnO rather than *p*-type GaN. Through use of Pulsed Laser Deposition (PLD) for this ZnO growth, the ultimate growth step could thus be performed at significantly lower Ts than is typically required for GaN growth in Metal-Organic Chemical Vapor Deposition (MOCVD). High crystallographic quality of the final hybrid LED structure and the integrity of the MQWs were confirmed by X-Ray Diffraction. The devices showed rectifying I/V characteristics with a turn-on voltage of 2.5 V and a discrete green Electroluminescence (EL) emission peaked at around 510 nm, which was readily visible to the naked eye. These results indicate that PLD-grown ZnO could be a good alternative to MOCVD-grown GaN for the *n*-type layer and that such inverted hybrid structures could hold the prospect for the development of green LEDs with superior performance.

In section 7 “Stranski-Krastanov growth of InGaN quantum dots emitting in green spectra”, we explain how to optimize InGaN quantum dots emitting in green spectra. In the 8th section, “Phosphor-free White Light-Emitting Diodes based on InGaN Quantum Dots”, we demonstrate room temperature white LEDs based on InGaN QDS.

In section 8 “Phosphor-free white light emitting diodes based on InGaN quantum dots”, we are demonstrating the optimization of green emitting InGaN quantum dots which are later integrated into LEDs. Thanks to the Stranski-Krastanov growth mode, white light emission is realized from these devices.

In summary, in this review we demonstrate the capabilities of III-Nitride devices emitting from ultraviolet through visible. We investigate novel hybrid green light emitting diodes as a means of cleaner green-light emission as well as develop quantum structures to be employed as active emitter material.

II. Ultraviolet Light Emitting Diodes

A. *Introduction*

The ultraviolet (UV) portion of the electromagnetic spectrum lies between visible light and X-rays, spanning the wavelength range of ~10 nm to ~380 nm. It may further be classified into near UV (200 nm < λ < 380 nm) and extreme or vacuum UV (10 nm < λ < 200 nm), or alternatively UVA (380-315 nm), UVB (315-280 nm), and UVC (<280 nm). The wavelength range of 240-280 nm forms a strategic window for unique applications on earth [1]. This is due to the fact that even though the sun emits radiation in this wavelength region, the earth’s atmosphere prevents these wavelengths from reaching the earth’s surface. Therefore, in this window, commonly referred to as the solar blind region, there is a naturally low amount of radiation. That is, the only UV light present on the earth’s surface in the solar blind region of the spectrum must be from a source on the earth’s surface. Since there are few natural sources of light in this wavelength range, there is a very low level of background noise for applications using these strategic wavelengths.

The development of UV emitters and detectors has been primarily driven by the military applications of chemical / biological agent detection systems and non-line-of-sight (NLOS) communications. Chemical / biological agent detection using UV emitters and detectors is done through fluorescence-based detection, while NLOS communication takes advantage of the solar-blind portion of the spectrum in order to achieve short range, covert communications.

In fluorescence-based detection, the characteristic fluorescence of biological markers intrinsic to biological agents is used to detect the presence of biological agents in the environment. An ultraviolet light source (preferably a laser) illuminates the cloud of the unknown agent in short pulses. If fluorescent biological markers are present, they will emit light at a wavelength slightly longer than the absorption wavelengths. This emitted light is then detected by a sensor with a peak detection adjusted to the characteristic fluorescence of the marker. The detected signal is then analyzed for each laser pulse: threat discrimination is based upon comparison of the signal to the background in order to detect significant changes in bioaerosols.

By combining semiconductor-based UV Emitters with photodetectors, it becomes possible to devise a compact system that can rapidly detect and discriminate amongst various biological agents based upon their fluorescence signature. For this, UV emitters and detectors at several strategic wavelengths are required. The choice of wavelength is dictated by the specific absorption and fluorescence of the corresponding biological markers. The UV light sources are selected to emit at the peak absorption wavelength of the bio-marker in question, for example at 280 nm for tryptophan, 274 nm for tyrosine, and 257 nm for phenylalanine – the three important amino acids with fluorescence properties – and ~340 nm for NADH. The resulting signal is subsequently collected by a photodetector band-pass filter set at the appropriate waveband corresponding to the florescence wavelength of the agent. The use of efficient semiconductor-based UV light sources would enable the overall system to be more compact, inexpensive, and portable with lower power consumption than current existing biological and chemical agent detection systems. Additionally, the reduced size and lower power consumption of the semiconductor UV sources will enable the incorporation of multiple excitation sources at different wavelengths in the same compact enclosure. The use of additional sources is expected to increase the specificity of the biological agent detection system by targeting specific fluorescence excitations from a variety of biological markers.

NLOS communication takes advantage of the solar blind region of the spectrum (λ<280 nm) for its very low background noise, high atmospheric scattering, and high absorption rate for UV signals. The very low background noise allows for easy signal detection; any UV signal less than 280 nm seen by the detector must be man-made. The high atmospheric scattering

allows for the signal to be transmitted without direct line of sight restrictions. The high absorption rate combined with the high atmospheric scattering leads to a strong extinction coefficient, which means that the signal cannot be detected from a distance, allowing for covert communications.

The system would consist of a transmitter unit with a UV source (wavelength of less than 280 nm) and a receiver with a solar-blind detector (cutoff wavelength of 280 nm). The receiver would be able to detect a signal from the transmitter as long as the distance between them is between approximately 10 and 250 meters. This form of covert communication would be invaluable to troop communication on the battlefield.

In addition to these two major defense applications, there are many civilian applications for UV emitters. Shorter wavelength lasers (into the UV end of the spectrum) would provide a means for higher density optical data storage and higher resolution laser printing, since the resolution of both of these applications is directly proportional to the wavelength of the laser. UV LEDs would enable fabrication of white LEDs for efficient, low cost lighting. UV-C light (100 nm < λ < 280 nm) deactivates the DNA of bacteria, viruses, and other pathogens, thus destroying their ability to multiply and cause disease. UV emitters in the UV-C range may be used for food sterilization and water / air purification. UV emitters may also be used for activation of photochemically sensitive resins and in-situ activation of drugs through optical stimulus.

Combinations of emitters and detectors would provide systems for free-space UV communications, and covert space communications, which would be secure from eavesdropping from anyone on earth.

UV detectors may be integrated into a watch or pager type device that could then be used to test for sun exposure, alerting the wearer when they had overexposed themselves to harmful UV rays. UV focal plane arrays (FPAs), or large arrays of mini UV detectors, provide UV imaging capabilities that have several possible applications. Visible and/or solar blind detectors eliminate a lot of background noise and thus FPAs made of such detectors are ideal for monitoring power lines for possible fault locations and UV flame detection and combustion monitoring in engines. The military desires solar blind UV FPAs for early missile threat warning, and aerial and terrestial UV countermeasures. UV astronomy would also benefit from UV FPA development.

For most of the applications described above, it is critical to have a compact and lightweight, chemically and physically robust UV detector and / or UV source in order to meet the needs of the applications and withstand the operating demands placed on the device. As will be discussed later, the nitride material system is uniquely matched to fulfill these demands.

The nitride material system has several important properties that make it ideal for visible to deep UV optoelectronic devices. These properties also allow InAlGaN material to withstand demanding applications that require harsh operating conditions.

The nitrides posses a wide band gap which, through alloying, can be tuned from about 0.9 eV for InN to 3.4 eV for GaN to 6.2 eV for AlN. This covers the wavelength range of IR radiation into to the deep UV end of the spectrum. III-Nitrides are the only semiconductor material system that covers the deep UV portion of the spectrum. Alloying allows for heterostructure devices, which improves device performance over a straight p-n junction. The III-nitride bandgap is a direct bandgap, which is ideal for optoelectronic devices.

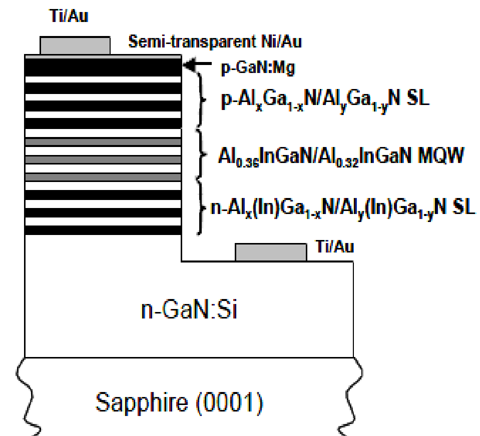

Fig. 1: Device structure of first 280 nm device.

(a)

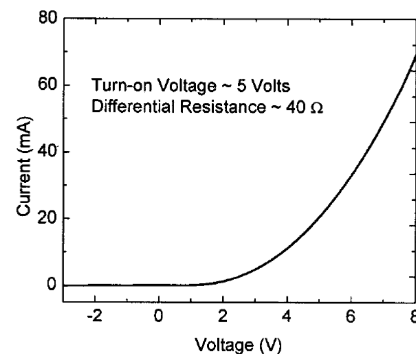

(b)

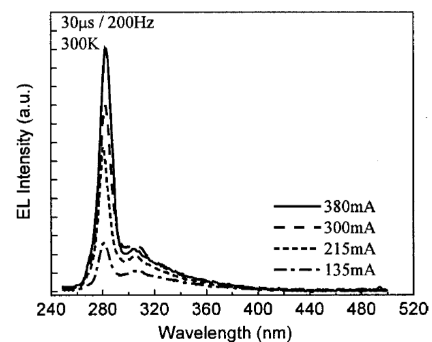

Fig. 2: (a) IV curve and (b) EL spectra of first 280 nm device.

B. First 280 nm LEDs

Our group achieved the first published 280 nm LED in early 2002 [2]. The structure, shown in Fig. 1, was based on AlInGaN / AlInGaN multiple quantum wells and was top-emission. The LED was fabricated using the 400 µm × 400 µm mask without a ring contact. The IV curve, shown in Fig. 2(a), demonstrates a turn-on voltage of approximately 5 volts, a differential resistance of 40 Ω, and reverse leakage at -3 V of approximately -10 µA. Fig. 2(b) displays the EL spectra at various pulsed mode currents, showing a peak emission wavelength of 281 nm for low current injection with a slight red-shift to 282 nm at higher injection currents.

C. High power 280 nm LEDs

In fall 2003, we demonstrated mW power from our 280 nm LEDs due to an improvement in material quality and device structure, as well as improvements in device geometry and packaging [3].

The device structure of the mW LED consists of an asymmetric single-quantum well (SQW) active layer confined between *p*- and *n*-type AlGaN on top of a high-quality AlGaN/AlN template. Deposition was initiated with a 20 nm low-temperature AlN buffer layer, followed by a 350 nm thick AlN layer, and a 30 period $Al_{0.85}Ga_{0.15}N$/AlN (50 Å/50 Å) superlattice topped with a 50 nm AlN layer. Next, 600 nm of Si–In codoped n-$Al_{0.5}Ga_{0.5}N$ was deposited forming the n-type contact layer which preceded a 100 nm thick n $Al_{0.45}Ga_{0.55}N$ layer. The active region consisted of a 10nm $Al_{0.4}Ga_{0.6}N$ barrier, followed by a 5nm $Al_{0.36}Ga_{0.44}N$ quantum well, and ending with a second 5 nm $Al_{0.4}Ga_{0.6}N$ barrier. A 10 nm $Al_{0.6}Ga_{0.4}N$ current blocking layer was then deposited to help prevent an overflow of electrons out of the active region. The asymmetric design of the active region is intended to compensate for the lower mobility of holes compared to electrons. This allows more of the injected electrons to contribute to recombination in the quantum well, which in turn increases the efficiency of the LED. The structure was completed with a 50 nm thick p-$Al_{0.45}Ga_{0.55}N$ layer followed by a 50 nm thick p-GaN contact layer. After growth, the sample was examined with both an optical and a scanning electron microscope and was found to be crack free. A schematic diagram of the device structure including the metallic contacts is shown in Fig. 3.

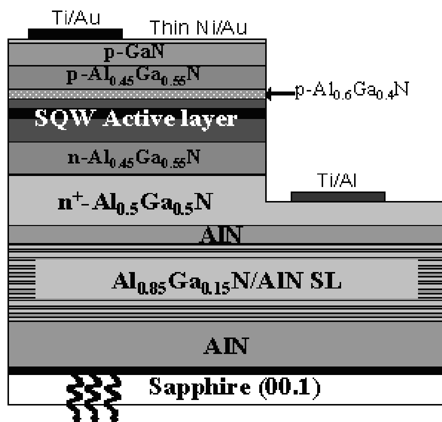

Fig. 3: Device structure of high-power 280 nm LED.

The standard deep UV LED fabrication process was utilized for these devices, using the 300 µm × 300 µm AlN submount set of masks in order to have a ring contact and be able to package the devices.

After processing, we analyzed the I–V characteristics of the devices. Fig. 4(a) displays the I–V curve of a single device, which has a series resistance of approximately 25Ω and a turn-on of approximately 6 V. By fitting the I–V curve an ideality factor of 5.6 is estimated. Next, we measured the EL spectra from a single diode under various pulsed injection currents (5 µs pulse width, 2 kHz frequency). These spectra, displayed in Fig. 4(b), demonstrate an approximately linear increase in intensity with increasing current. The dominant single peak occurs at ~280 nm. By fitting a Gaussian to the curve, we determined the peak to have a full-width at half-maximum value of 9.2 nm.

(a)

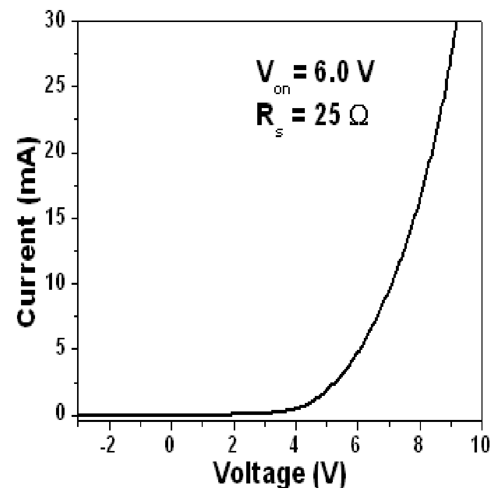

(b)

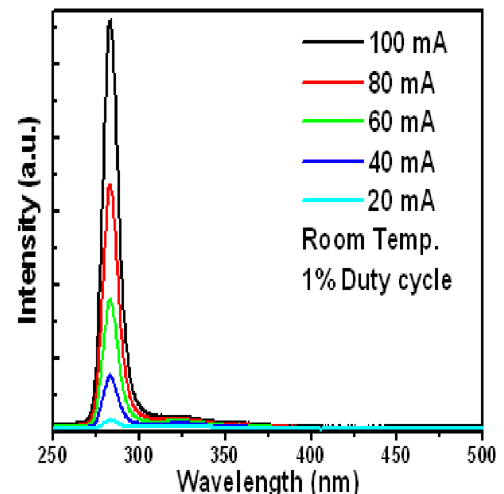

Fig. 4: (a) IV curve and (b) EL spectra of high-power 280 nm LED.

Finally, we measured the optical output power of the diodes. Fig. 5 shows the pulsed (200 ns, 200 Hz) P-I curve of a single diode and an array of four diodes connected in parallel.

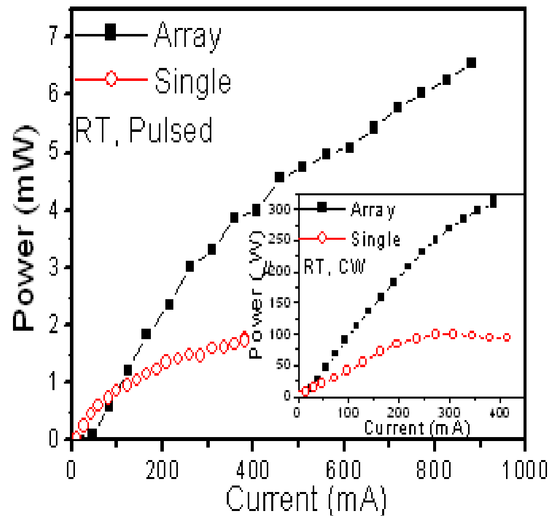

Fig. 5: Pulsed (200 ns, 200 Hz) P-I curves for a single device and an array of four devices. Inset displays the continuous wave power for a single devices and array of four devices.

Under 400 mA injection current, the output powers of the single diode and the array are 1.8 mW and 3.9 mW, respectively, with the array reaching a high power of 6.5 mW at 880 mA. The array is able to reach higher power at the same current as the single device because the current is spread across a larger area, which alleviates local heating effects. A clear decrease in slope efficiency is noticeable on both curves when comparing the low and high injection current regions. The curve for the diode array gives an initial slope efficiency of 14.7 µW/mA, which falls off to 4.8 µW/mA at higher current. This change is attributed to device heating caused by current crowding. The inset of Fig. 5 displays P– I curves measured under continuous-wave operation for both a single diode and an array of four diodes. At 300 mA, the single device and the array produced output powers of 100 µW and 270 µW, respectively. At 390 mA, the array reaches a power of 310 µW. Fig. 6 shows the EQEs corresponding to the P–I curves in Fig. 5.

Under pulsed current operation, the single device reaches a peak EQE value of 0.24% at a current of 40 mA while the array reaches 0.26% at 265 mA. After reaching the maximum value, the EQE curves roll off, a second demonstration of the decrease in device efficiency due to internal heating. The array reaches its peak efficiency at a later current because the current is spread across a larger area. However, after this peak value, the array EQE drops at a slower rate than the single device because, as discussed earlier, there is less localized device heating. Similarly, the continuous-wave EQE of the array reaches a higher value and stays relatively constant as compared to the continuous-wave EQE of the single device. The continuous-wave EQE curves reach peak values of 0.012% and

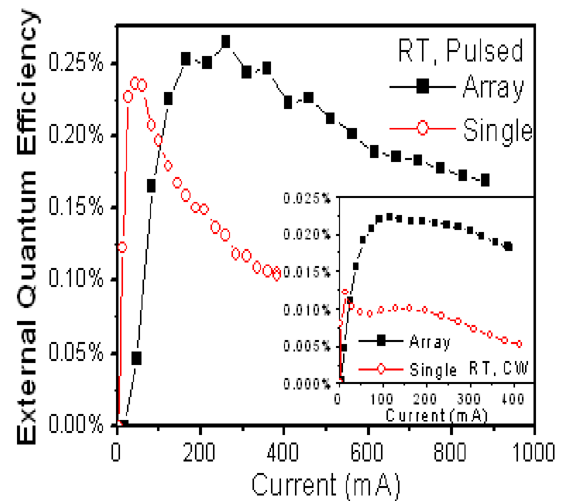

Fig. 6: External Quantum Efficiency (EQE) curves for a single device and an array of four devices under pulsed (200 ns, 200 Hz) current operation. The inset displays the EQE curves under continuous-wave operation for a single device and an array.

0.022% for the single device and the array, respectively.

D. LEDS with λ < 280 nm

(a)

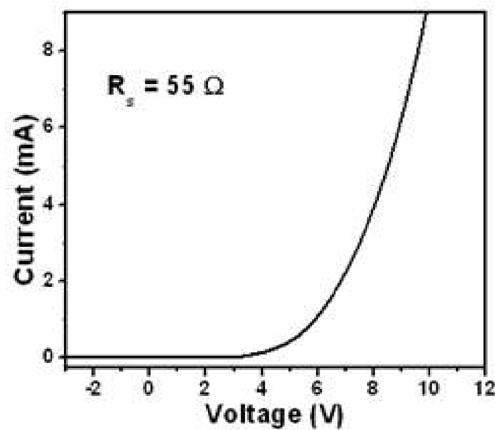

(b)

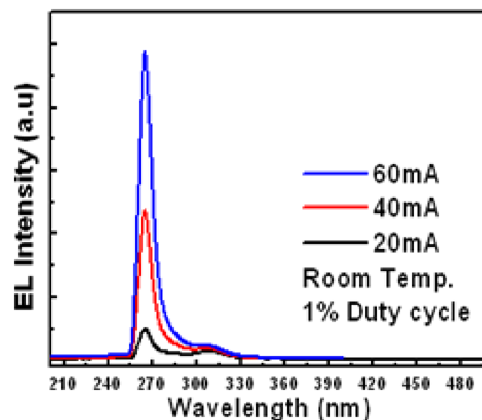

Fig. 7: (a) IV curve of a single 265 nm LED and (b) EL spectra at various currents showing a dominant peak at 265 nm [4].

At approximately the same time that we achieved high power 280 nm LEDs, we also achieved a similar result with 265 nm LEDs [4], and not long thereafter also achieved mW power from 250 nm LEDs, demonstrating our ability to produce high quality, high aluminum content AlGaN based devices, as well as successful device processing techniques applied to such difficult material. These devices were processed using the standard 300 μm×300 μm mask set and flip chip bonded to the AlN submounts.

The I-V curve for the 265 nm LED, shown below in Fig. 7(a), has a series resistance of 55 Ω with a turn-on voltage of approximately 6.5 V. The EL spectra, shown in Fig. 7(b), demonstrate a strong dominant peak at 267 nm that increases approximately linearly with increasing injection current, as expected, while the secondary defect related peak saturates with increasing current.

(a)

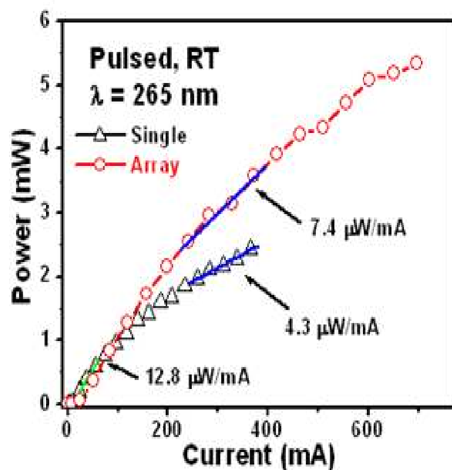

(b)

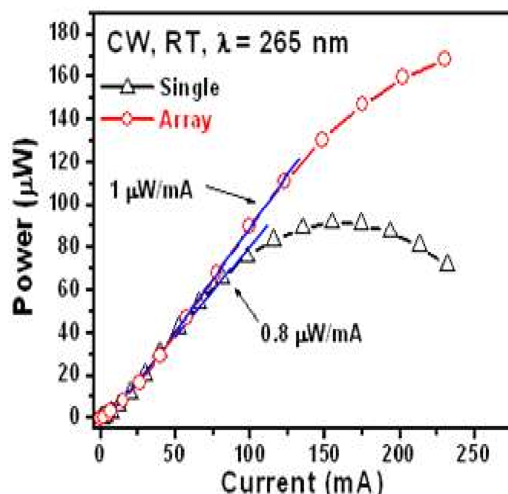

Fig. 8: (a) Pulsed P-I measurements of a single 265 nm diode and an array of four 265 nm diodes connected in series and (b) continuous wave measurements of a single 265 nm diode and an array of four 265 nm diodes connected in series

Fig. 8(a) shows the pulsed P-I curves of a single 265 nm LED and an array of four 265 nm LEDs connected in parallel. Both curves have an initial slope efficiency of ~12.8 μW/mA, however the single diode rolls off to a slope efficiency of ~4.3 μW/mA while the array is able to maintain a higher 7.4 μW/mA at the same current range. This is attributed to current spreading over more devices, which alleviates the localized heating effects. Thus, the array is able to reach 5.3 mW at a current of 700 mA.

Fig. 8(b) shows a similar trend for the continuous wave measurements from both a single 265 nm LED and an array of four 265 nm LEDs. Again, the array is able to avoid the thermal roll-over seen for the single device, which is attributed to current crowding causing device heating, in order to achieve a power of 170 μW at a current of 230 mA.

Similarly, the I-V curve for a single 250 nm LED, shown below in Fig. 9(a), demonstrates a series resistance of approximately 43 Ω, and a turn on voltage of ~10 V. The EL, shown in Fig. 9(b), has a strong single peak at ~254 nm.

Fig. 10 shows the P-I-V curves, measured under pulsed current operation (200 ns pulse at 2 kHz), for a single diode and an array of five diodes connected in parallel. It is clearly shown that the array has a much lower resistance than the single diode, as expected. The array clearly outperforms the single diode. This is again attributed to current spreading across the five diodes; due to the higher aluminum content and thus lower

(a)

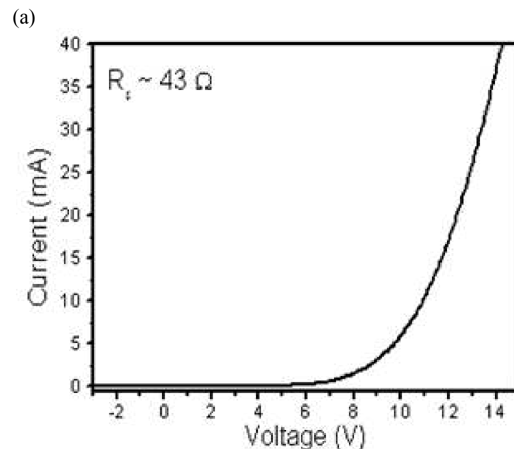

(b)

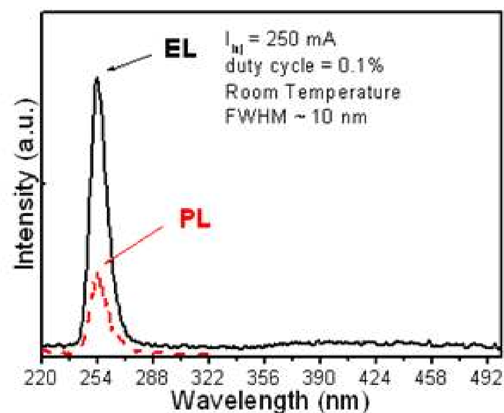

Fig. 9: (a) IV curve of a single 250 nm LED and (b) EL spectrum at an injection current of 250 mA of a single LED showing a single peak at 254 nm. The photoluminescence (PL) is shown for reference.

conductivity, current crowding becomes a much larger issue as the wavelength of the devices is lowered. Through connecting the devices in parallel, however, it was possible to achieve 3.2 mW at an injection current of 930 mA.

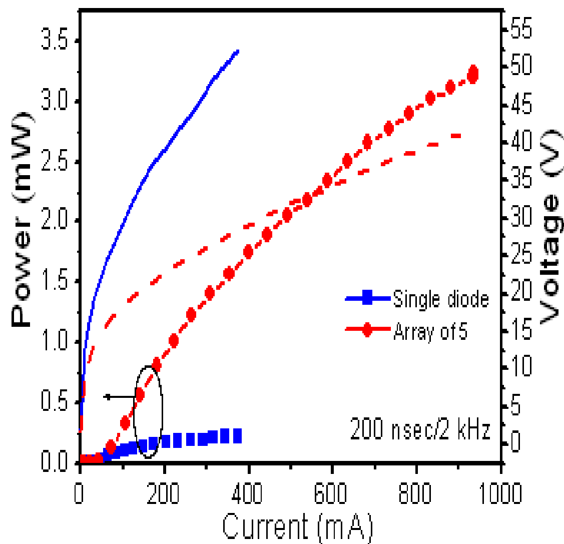

Fig. 10: P-I-V curves of a single 250 nm LED and an array of five 250 nm LEDs connected in parallel.

E. *Finger geometry / extended area UV LEDs*

The finger geometry / extended area UV LEDs demonstrated an improvement in performance through effectively decreasing current crowding, as shown by the near field image. This was confirmed by the wall-plug efficiency curve measured under continuous-wave operation, shown in Fig. 11.

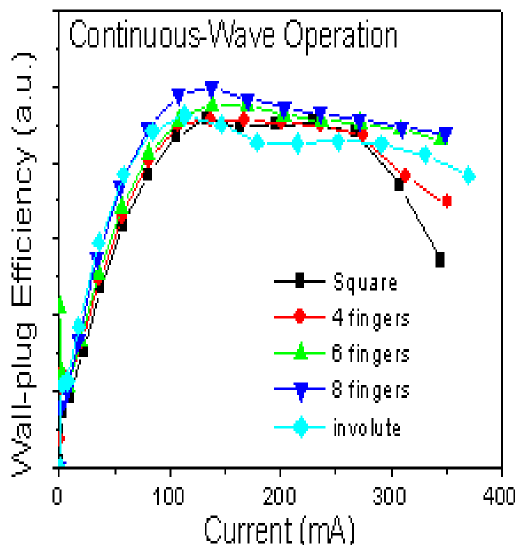

Fig. 11: Wall-plug Efficiency under continuous-wave operation for the 300µm x 300 µm square mesa, the four-, six- and eight-finger mesas, and the involute geometry mesa.

In Fig. 11, the square mesa and the four-finger mesa reach thermal roll-over at about 300 mA, after which the four-finger mesa slightly outperforms the square mesa. This was expected since the four n-type contact fingers should slightly reduce the current crowding by increasing the perimeter and thus the area that the current will flow through as compared the square geometry. The six- and eight-finger geometry and the involute geometry mesas do not reach a definitive thermal roll-over point, with the eight-finger geometry outperforming the six-finger geometry, again due to better current spreading with an increase in the number of n-type contact fingers, and therefore for an increased perimeter and current area.

F. *Micro-LEDs*

Preliminary microLED results indicating successful device improvements due to the RAE method have been achieved. Due to an inconsistency within the processing procedure, described below, the devices did not perform perfectly, however they do show a significant difference between the samples that cracked and the samples that were effectively crack-free.

Three pieces of the same sample were patterned for re-growth with the micro-LED mask set: a 12×12 piece, an 8×8 piece, and a 4×4 piece. The etch depth was ~1 µm so that the etch depth would be larger than the thickness of the re-grown device structure in order to take advantage of the RAE method. The three samples were then thoroughly cleaned using the process. The rest of the LED device structure was then grown on these three samples along with an un-patterned piece, for comparison.

After growth, the four pieces were examined by optical microscope. The 4×4 sample had cracks on the mesas, which was not unexpected since the mesa dimensions were at threshold size according to our RAE experiments. The un-patterned piece was also cracked, as expected. The 8×8 sample was found to have very few cracks on the mesas, and the 12×12 sample was to found to have virtually no cracking on the mesas.

Micro-LEDs were then fabricated on the four samples following a similar procedure, in order to insulate the thick p-type bonding contact from the n-type material. The un-patterned device was processed with the 8×8 micro-LED mask set, for comparison. The SiO_2 insulating layer was not uniformly etched during the buffered oxide etch step, and therefore windows through which to make contact to the p-type thin contacts on top of the mesas were not uniformly opened.

After processing, I-V curves of the devices were measured. The I-V curves revealed that the re-grown, crack-free 12×12 and 8×8 samples tended to have a sharper (less leaky) device turn-on and a lower differential resistance while the cracked 4×4 sample had a sluggish (leaky) device turn-on and a higher differential resistance, as shown in Fig. 12(a). When comparing the 8×8 re-grown sample to the 8×8 standard sample, the re-grown sample had a slightly lower turn-on voltage and lower resistance than the standard sample, as shown in Fig. 12(b).

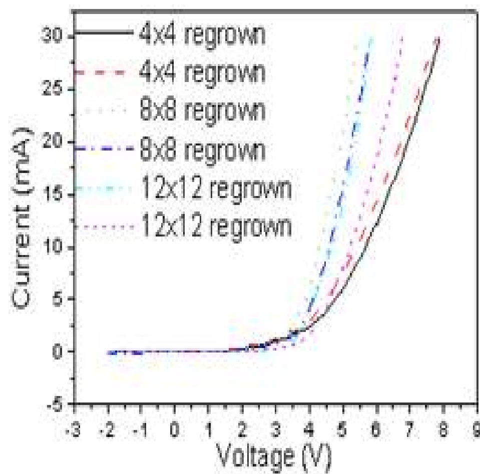

(a)

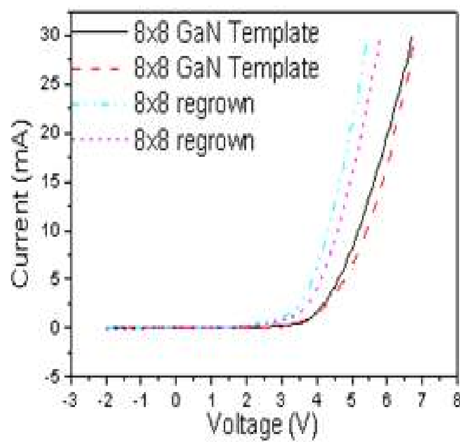

(b)

Fig. 12: Measured I-V curves for (a) the three re-grown samples, and (b) the re-grown 8×8 sample and the standard 8×8 sample.

Next, EL measurements were performed on the four samples. All displayed strong, single peak EL, however the peak wavelength tended to slightly shift between the samples, as displayed in Table 1.

TABLE 1: PEAK WAVELENGTHS OF THE MICRO-LED SAMPLES

Sample	Peak Wavelength
Standard (8×8 mask)	350.5 nm
4×4 re-grown	349.0 nm
8×8 re-grown	348.0 nm
12×12 re-grown	347.0 nm

This may possibly be attributed to the amount of strain induced in each situation. The amount of strain can roughly be correlated to the density of cracks present on the sample: the more cracks, the more strain relief, and thus the lower the strain. Similarly, the sample with the fewest cracks would have the highest strain. Therefore, the un-patterned standard sample, which appeared to have the highest crack density, would have the lowest strain, followed by the 4×4 re-grown sample and then the 8×8 re-grown sample, with the 12×12 regrown sample having the highest strain. The more strain, the thinner the device layers would be, and therefore the quantum well would be slightly thinner, shifting the energy levels up and the wavelength down.

Next, pulsed P-I measurements were taken. It should be noted that since the SiO_2 windows did not open uniformly, 100% of the mesas generally do not light up for each device. Since the three device designs were meant to all have the same overall mesa area, so that only the individual mesa size is varied, this processing issue does somewhat affect the comparison of the four devices. However, care was taken to perform P-I measurements on those devices with the highest percentage of mesas lighting up. These measurements, shown in Fig. 13, show that the 8×8 and 12×12 re-grown samples outperform the 8×8 standard and 4×4 re-grown samples; they are able to reach higher powers at a similar current, as well as reach higher currents without device degradation. This first observation, crack-free samples achieving higher power at a similar current, may be attributed to a combination of the following three scenarios: current crowding effects due to variance in individual mesa size, total device mesa area not lighting up due to processing difficulties, or device performance degradation

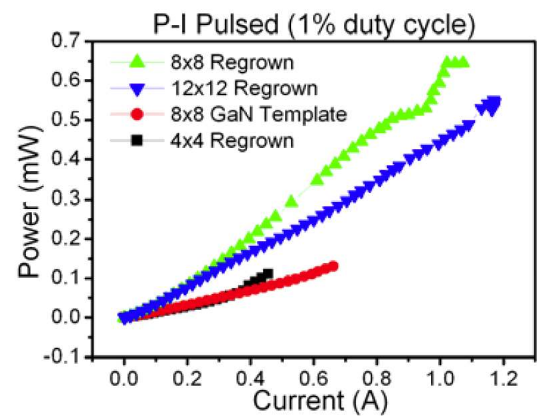

(a)

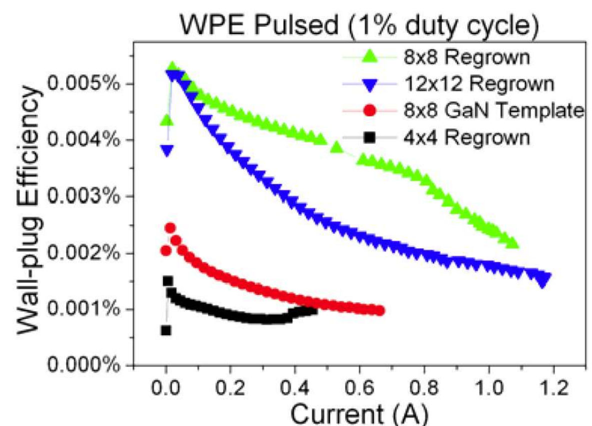

(b)

Fig. 13. (a) Pulsed P-I curves for the four samples and (b) corresponding WPE curves

due to cracking. In the case of the 4×4 re-grown device, since there is a significant difference in mesa size, current crowding may play a significant factor. It was observed via optical microscope that the 8×8 and 12×12 individual mesas light up much more uniformly than the 4×4 individual mesas. However, since this trend is also seen between the re-grown 8×8 sample and the 8×8 standard sample, it most likely also is partially due to cracking. The second observation, crack-free samples able to reach higher currents without device degradation, clearly demonstrates that the two samples with few to no cracks were able to outperform the samples with cracking since this observation is independent of output power; the RAE method was effective in improving device performance.

Fig. 13(b), the wall-plug efficiency for the four samples, also confirms this result. The two samples with little to no cracking reach a much higher WPE value than the two samples with cracking. Fig. 13(a) and (b) also show that the 8×8 re-grown sample outperformed the 12×12 re-grown sample. This may be due to the 8×8 re-grown LED lighting up more uniformly than the 12×12 re-grown sample, and therefore this result would need to be confirmed with an improved processing procedure.

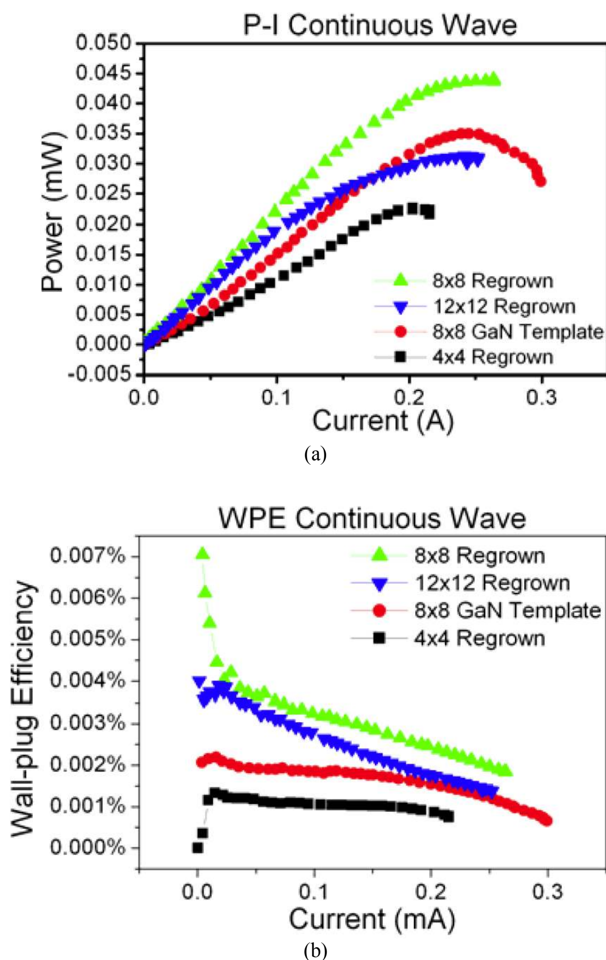

Fig. 14. (a) CW P-I curves for the four samples and (b) corresponding WPE curves.

A similar, yet less definite trend is shown by the CW P-I and corresponding WPE measurements, shown in Fig. 14(a) and (b). At lower currents, the 8×8 re-grown sample and 12×12 re-grown sample outperform the 4×4 re-grown sample and the 8×8 standard sample. However all four samples reach thermal roll-over at approximately 200-225 mA, with the 8×8 standard sample eventually reaching a higher power than the 12×12 re-grown sample. Again, this may be attributed to perhaps a slightly larger percentage of the total area lighting up, and therefore again, this result should be confirmed with a more reliable processing procedure.

G. *Conclusion*

Through an understanding into the processing procedures as they are applied to the III-nitride materials system combined with improvements to device geometry and packaging and the excellent material improvements made by my peers, many significant deep-UV emitter and detector technologies have been achieved. These include demonstration of first ever 280 nm LEDs,[2] demonstration of first ever RT milliwatt operation of 280 nm LEDs,[3] demonstration of first ever RT milliwatt operation of 265 nm LEDs,[4] and demonstration of RT milliwatt operation of sub-255 nm LEDs.

III. Hybrid Ultraviolet Light Emitting Diodes

A. *p-GaN / n-ZnO LED*

In early 2005, we were able to demonstrate a hybrid p-GaN / n-ZnO device [5].

The device was processed using the circular LED mask The device was first annealed to activate the acceptors in the p-GaN at 1000℃ in nitrogen ambient. Since ZnO is easily wet-etched by most acids, the photolithographically defined mesas were etched down to the p-GaN material via wet-etching with weak Acid solution. The photoresist was then removed and the sample was cleaned. The thin Ni/Au p-type contact was deposited using the ring contact mask for lift-off, followed by the standard anneal for the p-GaN contact. Next, a Ti/Au n-contact was deposited using the wire bonding contact mask, which was then annealed at 350℃ in nitrogen ambient. Finally a thick Ti/Au contact was deposited directly over the thin p-contact for wire bonding purposes, again using the ring contact mask for lift-off. Since ZnO is slowly etched in developer solutions and even very slowly etched by DI water, special care was taken in order to avoid damage to the ZnO whenever possible by minimizing its exposure to harmful chemicals.

The results from this hybrid LED are shown below in Fig. 15 (a), (b), (c), and (d).

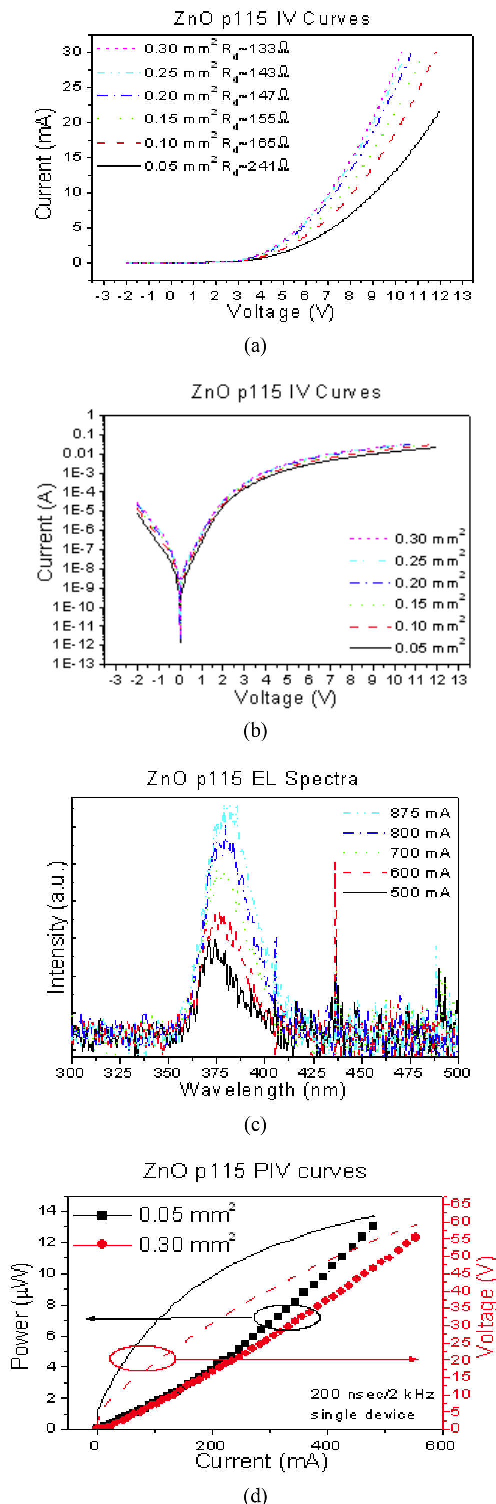

Fig. 15: (a) linear I-V curve of various sized mesas, (b) semi-logarithmic I-V curve of various sized mesas, (c) EL spectra at various currents, and (d) P-I-V measurements of the smallest and largest mesa sizes.

The I-V curves demonstrate a fairly constant turn-on voltage of approximately 5 V independent of mesa size, as well as a decrease in differential resistance with an increase in size. The reverse leakage current shows a slight increase with an increase in size as expected due to the increase of both area (possible bulk leakage) and circumference (possible edge leakage). The reverse leakages range from -7.06 µA at -2 V for the smallest sized LED to -28.2 µA at -2 V for the largest sized LED, which are fairly high values as compared to our non-hybrid LEDs. The EL demonstrates emission at a peak wavelength of approximately 374 nm at 500 mA and redshifts slightly with increasing current, approximately linearly, to about 382 nm at an injection current of 875 mA, attributed to device heating. This peak wavelength agrees with the photoluminescence spectrum, which had a peak wavelength of ~375 nm, and is characteristic of near-band-edge emission from ZnO. The P-I-V demonstrates ~12 µW peak power emission from both the largest and the smallest sized devices, which indicates that there is a good lateral homogeneity of the layer / device properties.

B. ZnO:N / n-Si LED

In June 2007, we observed rectifying behavior and discrete luminescence from a ZnO on n-Si LED structure. The ZnO was grown on n-Si substrates using pulsed laser deposition with a KrF excimer laser, as described elsewhere [6]. P-type conduction was targeted using N as a dopant. Photoluminescence, Hall measurements, and ECV measurements were performed, however the results were inconclusive as to whether the material was definitively p-type, and therefore it was decided that device characterization would be used to further investigate.

After material characterization, the sample was annealed in order to activate the ZnO:N material. Mesas were then defined via photolithography and a wet etch in a dilute phosphoric and acetic acid solution [7]. A Pt / Ni / Au contact was then deposited and annealed in order to form an ohmic contact to the ZnO:N [8]. Finally, a Ti / Au contact was deposited on the n-Si as the n-type ohmic contact [9]. Prior to deposition, the n-Si surface was subjected to a brief buffered oxide etch in order to minimize the SiO_2 barrier between the semiconductor and the metallic contact. The cross section of the device structure is shown schematically in Fig. 16.

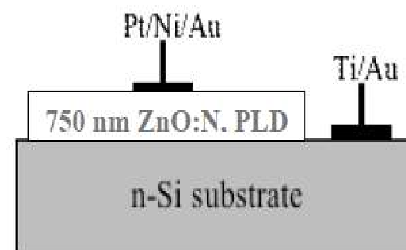

Fig. 16: Cross-sectional schematic of the ZnO:N / n-Si heterojunction device structure.

Following device processing, electrical characterization of the devices was carried out. The inset of Fig. 17 shows the I-V curve of the Pt / Ni / Au contact, demonstrating that a good ohmic contact is formed on the ZnO:N material. The linear IV curve of a device with a mesa area of 0.15 mm^2 is displayed in Fig. 17, demonstrating rectifying behavior. A linear fit to the

higher voltage regime of this curve allows for the calculation of a differential resistance of 99 W and a turn-on voltage of 3.36 V. This turn-on voltage corresponds to the ZnO band gap, suggesting a junction with electron injection into the ZnO. Through modeling of the I-V curve in the high current regime, a series resistance of 56 W was found. A linear fit to the low current regime of this I-V curve in log scale results in the determination of an ideality factor of n = 2.34 for this diode [3].

This value, which lies slightly outside of the expected range of 1 < n < 2, indicates that an additional process is contributing

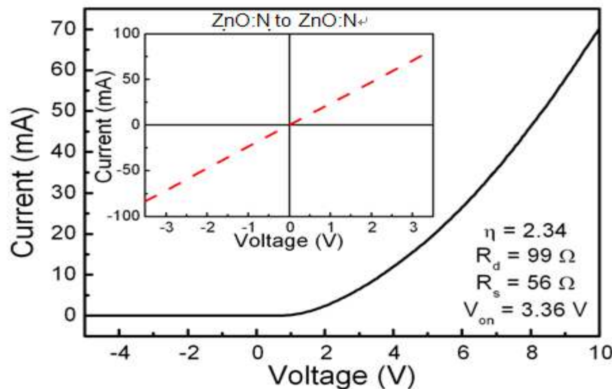

Fig. 17: RT I-V characteristic for a 0.15 mm^2 mesa structure. Inset displays the I-V curve for a ZnO:N to ZnO:N contact metallic contact, demonstrating ohmic behavior.

to the conduction in the diode.

The I-V curve of this same device in log scale is shown in Fig. 18. This curve demonstrates relatively low reverse leakage,

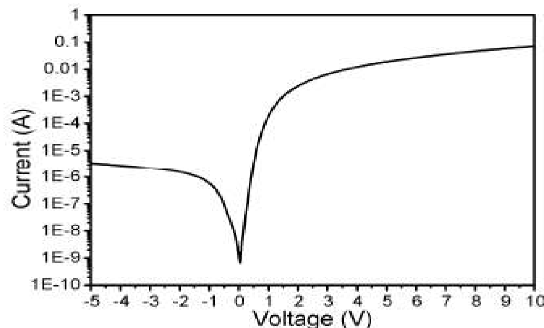

Fig. 18: RT log (I-V) characteristic for a 0.15 mm^2 mesa structure.

with a dark current density of 2.24 mA /cm^2 at -5 V.

For currents over 1mA, electroluminescence of the mesa was observed with a main broadband emission centered at about 600 nm plus a small 380 nm peak, which corresponds to the energy of ZnO near band edge. The relatively low injection current at which this luminescence appears (~30 mA) indicates that the luminescence is not due to impact ionization. An image of the top view of a 0.05 mm^2 mesa under 0 V bias is shown in Fig. 19(a), while Fig. 19(b) is a picture of the same diode (in the dark) with an injection current of approximately 100 mA operated under DC bias. This image shows the electroluminescence of the mesa, with discrete spots which were visible to the naked eye. Experiments on similar samples grown in the absence of nitrogen showed no light emission.

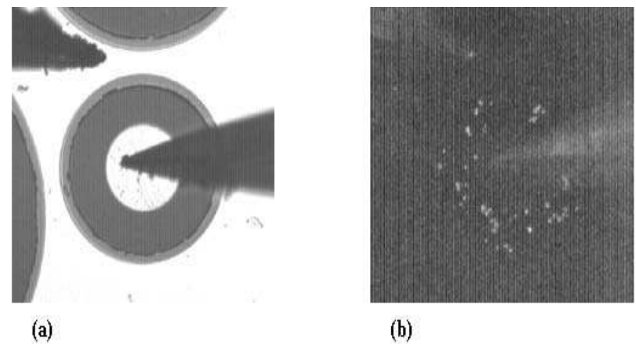

Fig. 19: (a) Image of the mesa while being probed for electrical characterization. (b) Image of the mesa operated under DC bias with a current injection of approximately 100 mA demonstrating electroluminescence from discrete spots within the mesa area.10

IV. Comprehensive Study of Blue and Green Multi-Quantum-Well Light Emitting Diodes Grown on Conventional and Lateral Epitaxial Overgrowth GaN

A. Introduction

Solid state lighting (SSL) holds the promise of a more energy-efficient, longer-lasting, more compact, and lower maintenance substitute for today's incandescent and fluorescent light sources. Since lighting currently represents about 22% of all electricity consumption, the adoption of SSL could significantly reduce greenhouse gas emissions. [11] Light-emitting diodes (LEDs) based on InxGa1-xN alloys, are currently the most promising candidates for realizing efficient SSL. InGaN is a direct wide bandgap semiconductor with an emission which can span the entire visible spectrum via compositional tuning. However, InGaN LED performance is highly wavelength-dependent. Indeed, ultra-bright and efficient blue InGaN-based LEDs are readily available [12] but the efficiency of InGaN-based green LEDs is still far from adequate for use in SSL. [13], [14], [15]

The lack of economical lattice-matched substrates for the growth of III-Nitrides necessitates the usage of GaN-mismatched silicon carbide (SiC) or sapphire (Al_2O_3) substrates, which leads to dislocation densities on the order of 10^8 cm^{-2}. The high performance of blue LEDs in spite of these dislocations is attributed to indium segregation in the InGaN layers that produces nanometer-wide indium-rich regions that behave like quantum dots. [16], [17] These quantum dots (QDs) localize the carriers, and prevent them from recombining non-radiatively at the dislocation sites. [18],[19] Difficulty in realizing high power green LEDs has three major parts (1) the limited solubility of indium in InGaN [20] imposes a restricted growth window for the green-emitting InGaN active layer, (2) InGaN with high indium content becomes unstable at elevated growth temperatures required for other layers in the device [21] leading to indium migrating out of the active layers, which reduces the LED spectral quality, [14],[21] (3) InGaN with high indium content generates dislocations leading to lower performance. [22]

Blue and green LEDs grown on conventional GaN have been compared in order to study the wavelength-dependent device performance. [23], [24], [25] Blue LEDs and laser diodes (LDs) grown on LEO GaN have also been studied in other works, showing superior performance to those grown on conventional GaN. [26], [27] Devices on LEO GaN offer lower leakage current [26], [28], [29], higher stability, better thermal properties [27], and longer device lifetime. [30] Despite these advantages, there are no studies of green active layers and LEDs on LEO GaN. In this work, we analyze blue and green active layers on conventional and high quality LEO GaN by X-ray diffraction (XRD), atomic force microscopy (AFM) and photoluminescence (PL). Then, we integrate them into LEDs, compare and correlate the material characteristics and device performance [31].

B. Experiment

1) Growth and Material Characterization

MQWs and LEDs were grown on double side polished c-plane sapphire substrate in an Aixtron 200/4-HT, horizontal flow, low pressure, metal organic chemical vapor deposition (MOCVD) reactor. Trimethlyaluminum (TMAl), Trimethylgallium (TMGa), and Trimethlyindium (TMIn) were the metalorganic cation precursors for Al, Ga, and In sources, respectively. Bis(cyclopentadienyl)magnesium (Cp_2Mg) and Silane (SiH_4) were used as the p-and n-type doping sources, respectively. Ammonia (NH_3) was used as the nitrogen anion source. Nitrogen was used as the carrier gas for growth of the MQWs to help increase indium incorporation whereas hydrogen was used during the rest of the layers.

2) Preparation of high quality LEO GaN

Growth began with desorption of the sapphire substrate at 1100ºC under H_2. Then, a thin low-temperature GaN buffer layer was grown, followed by 2 µm of GaN, grown at 1050ºC. In order to create a mask for lateral overgrowth, the wafer was removed from the reactor and 50 nm of silicon nitride (SiN) was deposited by plasma enhanced chemical vapor phase deposition (PECVD) [32] and patterned along the GaN <1 -100> direction with openings of 2 µm and a period of 15 µm. This pattern direction exposes the A-planes (11-20) for lateral growth and is known to give fastest lateral growth rate and high quality wing regions.[33] For higher device performance, smaller fill factors (ratio of mask opening width to stripe period) are desired, which makes regrowth more challenging. [34] We have used a fill factor of 0.13 to have a larger wing area and to perform better analysis.

Etching of the opening in the SiN layer was performed by electron cyclotron resonance reactive ion etching (ECR-RIE) using an SF_6 based chemistry; we have observed that this ECR-RIE chemistry does not etch GaN appreciably, however, some surface damage is observed by scanning electron microscope (SEM). Some SiN residuals were observed on the GaN opening regions via AFM. However, when GaN regrowth tests were conducted in these opening regions, a smooth GaN surface was observed via SEM, showing that slight remaining SiN residues did not have a detrimental effect on the GaN

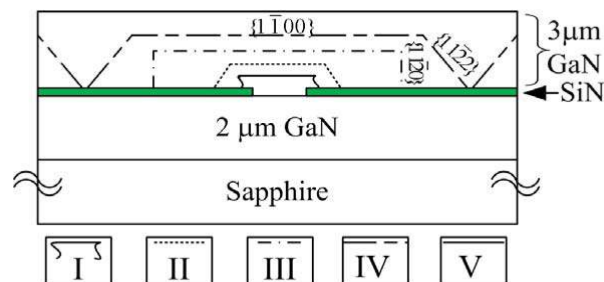

Fig. 20: Schematic sketch of our optimized five-step LEO GaN growth process.

regrowth. Proper trade-off must be made between etching time and surface damage, and amount of SiN residual atoms in the GaN opening in correlation with the regrowth characteristics.

After etching, samples were cleaned with trichloroethylene, acetone, methanol, and rinsed thoroughly. Then, samples were placed inside the reactor for our optimized five-step LEO GaN re-growth. A cross-sectional sketch of the LEO GaN steps is shown in Fig. 20.

Step I is designed for high surface diffusion to minimize nucleation on the SiN mask and promote vertical growth on the GaN in the SiN openings in order to create an initial well-formed seed from which the vertical growth will progress. The vertical thickness should be around double the SiN layer thickness. Important growth parameters such as growth temperature, V/III ratio, effective lateral to vertical growth rate ratio, and growth time are given in Table 2.

Step II is similar to Step I except the growth conditions are adjusted to favor both lateral and vertical growth in order to obtain straight side walls. [35] Growth temperature is increased and V/III ratio is decreased, as given in Table 2. If Ga and N adatoms are too mobile, then they tend to align themselves exactly as the etching pattern. However, since the edges of the SiN mask are not perfectly straight lines, this step is needed to achieve better straight sidewalls. At the end of this step well formed inclined {11-22} facets are observed.

Step III is the lateral growth phase, during which the lateral to vertical (L/V) growth rate is enhanced by increasing the growth temperature. [34] Increasing effective lateral to vertical growth rate ratio (L/V) decreases the growth time required for coalescence, and helps bend the threading dislocations sideways.[33] During the first part of Step III the initially inclined {11-22} sidewalls begin to tilt, and are replaced with vertical {11-20} sidewalls (Fig. 20). This change in the growth direction over the first three steps, from vertical to lateral, helps to bend the threading dislocations sideways so that they do not propagate to the surface.

Step IV is the coalescence step; after the distance between the side walls is close enough, the side wall slope is increased, as shown in Fig. 20 in order to realize a void free coalescence front. This is achieved by decreasing the growth temperature sufficiently so that growth favors the formation of inclined {11-22} facets. [34] This inclination minimizes the voids and prevents the dislocations spreading at the coalescence front. Failure to control the lateral to vertical growth rate during coalescence results in the formation of voids and leads the LEO GaN surface to bend, both can be observed by SEM. During

this phase, the lower temperature necessary to realize inclined planes results in less surface diffusion, and the lack of exposed SiN removes the supply of excess adatoms at the facet edge. [36] This results in a slow lateral growth rate, requiring a longer time for full coalescence.

Step V is similar to conventional GaN growth and promotes vertical growth. N-type doping is achieved by introducing SiH_4 during in this step, as LEDs will be grown on this template. Typically up to 0.6 µm is grown in this layer. The GaN vertical growth height at full coalescence is ~5 µm, small enough that

TABLE II
IMPORTANT GROWTH PARAMETERS FOR LEO GAN
(2 µm opening 15 µm period)

LEO Step No:	T_{growth}(ºC)	V/III Ratio	L/V Ratio	t_{growth} (mins)
I	1080	6000	1.1	4
II	1100	2930	2.4	60
III	1130	2930	2.6	60
IV	1100	2930	1.4	195
V	1040	2400	1.0	30

LEO Step number, growth temperature (T_{growth}(ºC)), V/III ratio, effective lateral to vertical growth rate ratio (L/V), and growth time (t_{growth}).

wafer bending effects are minimal. [37]

Table 2 summarizes the basic growth parameters for the above explained five-step LEO growth process (Fig. 20) for an opening of 2 µm and period of 15 µm. It should be possible to reach high quality LEO GaN for different filling factors and

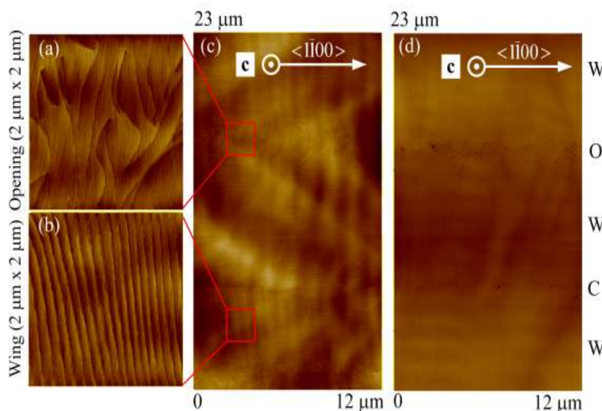

Fig. 21. AFM images of coalesced LEO GaN. (a) opening (2 µm x 2 µm) and (b) wing (2 µm x 2 µm) have root mean square (RMS) roughness of 1.9 Å and 1.5 Å, respectively. (c) displays larger area (12 µm x 23 µm) AFM scan. (d) displays dislocations, revealed by hot phosphoric acid treatment, which are seen as dark spots. 'W', 'O' and 'C' corresponds to wing, opening and coalescence regions, respectively.

periods, by employing the ideas described in each growth step.

Fig. 21 displays the AFM of the fully coalesced LEO GaN templates. The surface above the opening region (Fig. 21(a)), is similar to that of conventional GaN, exhibiting chaotic atomic steps, the surface termination of which identify screw/mixed type threading dislocations. [36] Contrarily, the wing region (Fig. 21(b)), where lateral growth occurs, possesses well ordered parallel atomic steps with no atomic step terminations. The entire surface, including the coalescence region, where the neighboring atomic steps interfere, is observed in Fig. 21(c). In order to study the dislocations, a hot (170ºC) phosphoric acid (85% H_3PO_4) treatment [29], [38] for 15 minutes was used. This etch-pit-density study reveals no discernable dislocations in the wing areas, whereas in the LEO GaN coalescence area, and opening region dislocation densities of (2±1) × 10^8 cm^{-2}, and (9±2) × 10^8 cm^{-2} are observed, respectively (Fig. 21(d)). For comparison, conventional GaN was observed to have a dislocation density of (9±1) × 10^8 cm^{-2}. This phosphoric acid treatment is capable of distinguishing between edge and screw or mixed type dislocations. [29], [38] The bigger pits correspond to dislocations with screw component whereas smaller ones correspond to edge type dislocations. It is know that edge type dislocation may exist in the wing region as their bending is very sensitive to growth conditions. [39] The non-existence of any discernable dislocations on our wing regions show the quality of the five-step LEO GaN developed, and establish a baseline from which we can study the effect of dislocations on blue and green InGaN based LEDs. For LEO GaN, no GaN peak separation is observed (in Fig. 22) which shows that there is no significant plane tilt [40], supporting our high quality growth scheme described.

After preparation of LEO templates as described above, blue and green MQWs and LEDs are grown simultaneously on these templates, and on conventional GaN for comparison purposes. Each quantum well was composed of 3.5-nm-thick InGaN with a 7.0nm-thick GaN barrier. The thicknesses of the blue and green MQW layers are arranged to be the same in order to have a better comparison. Growth temperatures of the MQWs are adjusted to ensure blue and green luminescence from the InGaN QWs. These MQWs were capped with 550 nm thick p-GaN complete the LED structure.

3) Blue and green active layers on conventional and LEO

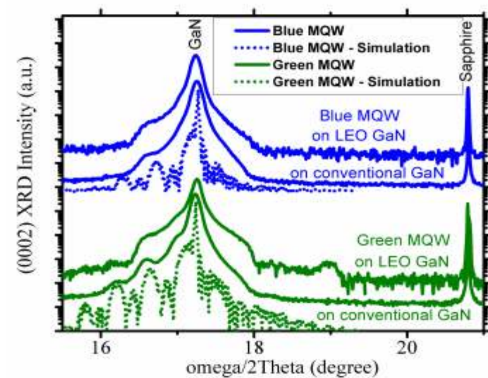

Fig. 22. (0002) XRD omega/2Theta scan of blue and green MQWs on conventional and LEO GaN. The XRD simulation is realized to compare with experimental results.

GaN

Open detector X-ray diffraction (XRD) studies and XRD simulations are carried out to confirm the indium composition, and InGaN and GaN thicknesses of the active layer. Fig. 22 displays the (0002) XRD (omega/2Theta) scan for blue and green three-MQWs on LEO and conventional GaN. The XRD

simulations of these MQWs are also plotted, and show good agreement with the experimental data. The InGaN and GaN thicknesses are determined as 3.5 and 7.0 nm, respectively. The indium content in the InGaN well is calculated to be 20% for blue MQWs and 28% for green MQWs. The 0th order MQW peak is more distinctly observed in green MQWs due to higher average indium content in these structures.

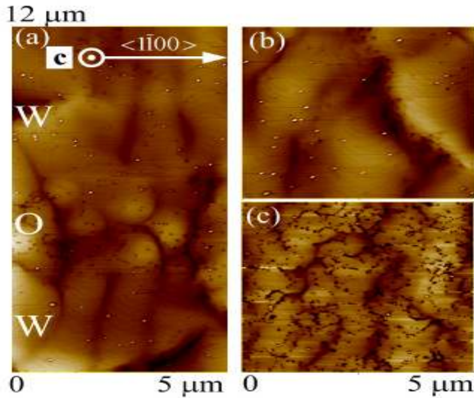

Fig. 23. AFM images of blue MQWs on (a) LEO GaN (5 μm x 12 μm), (b) wing area of LEO GaN (5 μm x 5 μm), (c) conventional GaN (5 μm x 5 μm). 'W', and 'O' corresponds to the wing and opening regions, respectively.

Atomic force microscopy is used to study the surface morphology of the MQW active layers. Fig. 23 shows the AFM images of the last barrier of blue MQWs on LEO and conventional GaN. Screw type threading dislocations are observed to be dominant on the opening (Fig. 23(a)). Fig. 23(b,c) show that active layer on wing area has much fewer dislocations and a much smoother surface than that on conventional GaN. This is directly related to the lower dislocation density in the wing area. Fig. 24 shows the AFM images of green MQWs on LEO and conventional GaN. Screw type dislocations are still dominant in the opening region. Although less dislocations are observed on the wing than that on the conventional GaN (Fig. 24 (b,c)), an island-like (2-D) growth is observed to be dominant across the LEO stripe , different from the blue active layer case (Fig. 23). The lower deposition temperature necessary to realize a green active layer results in an island-like growth rather than a layer-by-layer growth as was observed for blue layer. In summary, the wing regions are observed to be smoother than opening regions.

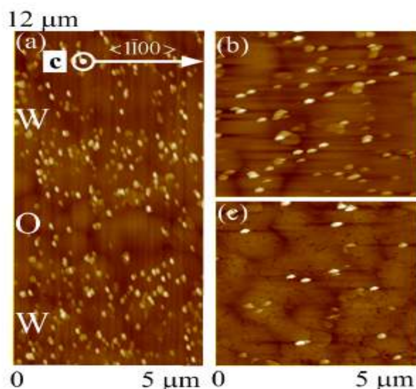

Fig. 24. AFM images of green MQWs on (a) LEO GaN (5 μm x 12 μm), (b) wing area of LEO GaN (5 μm x 5 μm), (c) conventional GaN (5 μm x 5 μm). 'W', and 'O' corresponds to the wing and opening regions, respectively.

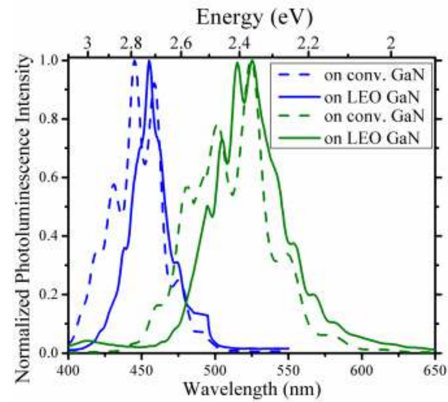

Fig. 25. Room temperature PL of blue and green active layers.

Room-temperature (RT) photoluminescence of these blue and green emitting MQWs are shown in Fig. 25. The PL wavelength of MQWs on LEO GaN is observed to be slightly higher than that of the same structure grown on conventional GaN. This could be due to increase in *c*-plane lattice constant of LEO GaN [41], leading to a smaller compositional pulling effect [42], thus allowing slightly more indium into the InGaN.

4) Fabrication of blue and green LEDs

Blue and green active layers composed of seven-MQWs were grown as described above with the addition of a 550 nm thick p-GaN capping layer to complete the LED structure. Activation of the p-type GaN is achieved by rapid thermal annealing (RTA) at 1000ºC for 30 s in nitrogen ambient. After this the surface is treated with $HCl:H_20$ (1:1), 30Å Ni/ 30Å Au is deposited and annealed for 10 mins under air to achieve a transparent ohmic contact to p-GaN. ECR-RIE ($SiCl_4$:Ar based chemistry) is used to etch 300 μm x 300 μm mesas, thus, each LED mesa spans many opening, wing, and coalescence regions. Finally, 400Å Ti/1200Å Au is deposited as a thick n-type contact and to serve as a central bond pad on top of the thin transparent p-contact in order to complete the LED fabrication.

C. Device Results and Discussions

The blue and green LED on conventional GaN are hereinafter referred as "B_{Conv}." and "G_{Conv}." whereas those on LEO GaN as "B_{LEO}" and "G_{LEO}", respectively. Fig. 26(a, b) show the I-V curves of blue and green LEDs on conventional and LEO GaN. A clear improvement in reverse-bias leakage characteristics is observed between samples B_{LEO} and B_{Conv}. whereas no significant difference is observed between samples G_{Conv}. and G_{LEO}.

Reverse bias characteristics of the LEDs are studied in detail. The majority of the leakage current is expected to flow through the LED, with only a small portion contributed by surface leakage. [43] The leakage current through nitride p-i-n devices is known to be dominated by hopping of charged carriers via localized defect-related states (traps) in the depletion region. [44], [45] In the case of defect dominated reverse conduction, the reverse I-V characteristics of LEDs can be modeled as[29]

$$I = I_0 e^{qv/e_0} \quad (1),$$

where V and E_0 are the diode voltage and the energy parameter, respectively, with I_0 being a pre-exponential factor. E_0 represents the electrical activities of dislocations with a screw component, and is known to be dependent on the voltage at which the fitting is realized [29], [44], [45]. For electrical fields E << (2kT/qa) ≈ 5×10^5 V/cm (assuming a, the localization radius of the electron wavefunction, is 10 Å), thermionic emission over a barrier dominates the leakage current. [28] We have used the fitting at low voltage range (1 < V < 5). In this range, I_0 and E_0 are related to the density and to the electrical activities of dislocations with a screw component, respectively. [29], [43], [44], [45], [46] Using Eqn. (1) to fit the I-V curves, reverse bias parameters I_0 and E_0 are calculated, and given in Table 3.

TABLE III
IMPORTANT CALCULATED/FITTED LED PARAMETERS

Identifier	Device	I_0 (μA)	E_0 (eV)
$B_{Conv.}$	Blue LED on conventional GaN	7.86×10^{-6}	1.34
B_{LEO}	Blue LED on LEO GaN	3.17×10^{-10}	0.73
$G_{Conv.}$	Green LED on conventional GaN	2.01×10^{-6}	0.91
G_{LEO}	Green LED on LEO GaN	2.16×10^{-6}	0.80

leakage current pre-exponential factor (I_0), electrical activities of dislocations with a screw component factor (E_0).

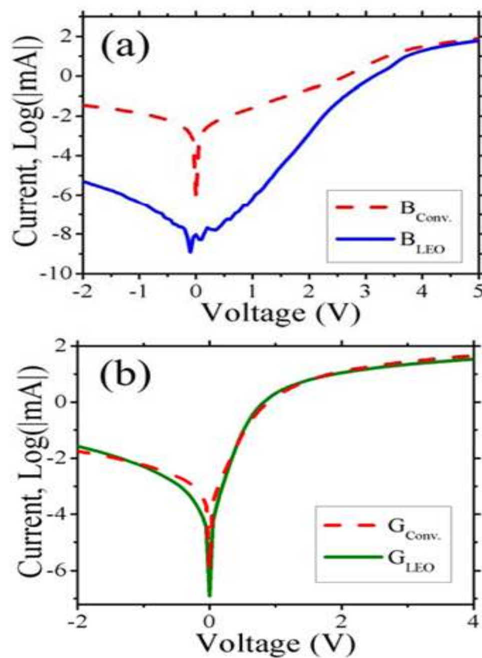

Fig. 26. Current-Voltage curves (logarithmic scale) of blue and green LEDs on conventional ($B_{Conv.}$, $G_{Conv.}$) and LEO GaN (B_{LEO}, G_{LEO}).

I_0 is related to square of the density of dislocations with a screw component. [29] Comparing I_0 values among the different samples in Table 3 suggests B_{LEO} has approximately two orders of magnitude lower dislocation density than $B_{Conv.}$. This agrees with the etch-pit-density study of the LEO GaN (Fig. 21). For $G_{Conv.}$ and G_{LEO}, no significant difference in I_0 is observed. As the same LEO GaN templates are used for B_{LEO} and G_{LEO}, the active layer used in samples $G_{Conv.}$ and G_{LEO} is the dominant dislocation generator leading to uniform dislocation distribution through the active layer. This helps explaining why we do not see a significant difference in I_0 between samples $B_{Conv.}$, $G_{Conv.}$, and G_{LEO}.

E_0 is very sensitive to the growth conditions [29] thus blue ($B_{Conv.}$ and B_{LEO}), and green ($G_{Conv.}$ and G_{LEO}) emitters should be considered separately. The lower value for sample B_{LEO} compared to $B_{Conv.}$ could be due to periodic alignment of the dislocations leading to a stronger voltage dependency of leakage current. A similar trend is observed between G_{LEO} and $G_{Conv.}$; however, it is less pronounced, due to the generation of additional dislocations in the active layer creating an almost homogeneous dislocation density similar to conventional GaN (Fig. 23, Fig. 24). The higher active layer quality of sample $B_{Conv.}$ compared to $G_{Conv.}$ could be the reason for higher value of E_0 leading to smaller dependency of leakage current on voltage.

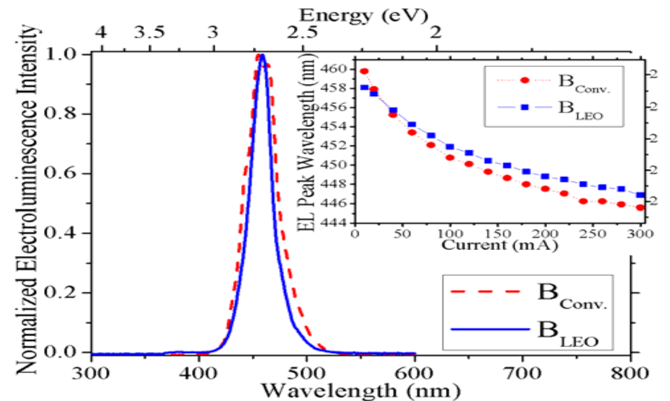

Fig. 27. Electroluminescence spectra of blue LED on conventional ($B_{Conv.}$) and LEO GaN (B_{LEO}) under 20 mA current injection. Inset displays the peak wavelength at different current injections.

Electroluminescence (EL) spectra were acquired for the LEDs under pulsed current injection (duty cycle of 10% and frequency of 5 kHz) in order to help reduce heating effects under higher current injection (Fig. 27, Fig. 28). The minimal role heating was confirmed by measuring the peak intensity versus power and noting that, for the currents used in this study, no thermal roll-over was observed to occur. The EL spectra of blue LEDs are shown in Fig. 27. The inset shows that both devices demonstrate a blue shift (from 465 to 446 nm) with increasing current. The decrease in wavelength with injection current is attributed to bandgap renormalization (due to free carrier screening of the piezoelectric (PE) field). At all but the lowest currents, B_{LEO} has a slightly longer wavelength emission than $B_{Conv.}$ (Fig. 27 inset). In previous blue LED studies, a similar observation has been reported. [26] This observation is

in agreement with the PL that was discussed in section II(b). Device B_{LEO} has a narrower EL spectra then B_{Conv}. (Fig. 29). This suggests a more uniform indium distribution throughout the active layer. [17] Indeed, Fig. 23 directly illustrates the more uniform surface of blue MQWs on LEO GaN, supporting

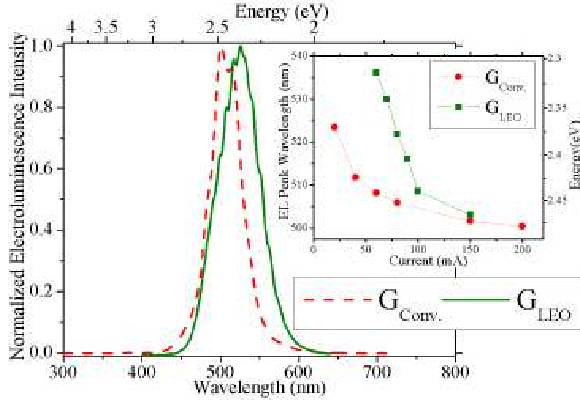

Fig. 28. Electroluminescence spectra of green LED on conventional (G_{Conv}.) and LEO GaN (G_{LEO}) under 80 mA current injection. Inset displays the peak wavelength at different current injections.

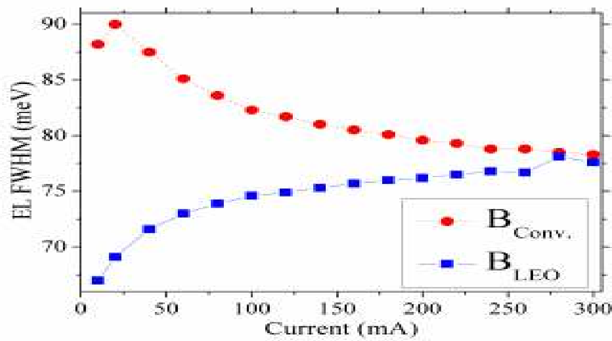

Fig. 29. EL FWHM dependency on current for blue LED on conventional (B_{Conv}.) and LEO GaN (B_{LEO}).

the advantage of LEO templates.

In Fig. 29, the EL FWHMs of the blue LEDs are plotted as a function of the injection current; the FWHM of device on conventional GaN can be seen to decrease with current, while the FWHM of the device on LEO GaN can be seen to increase. The EL FWHM broadening in B_{LEO} could be related to dislocation alignment in the LEO openings resulting in an

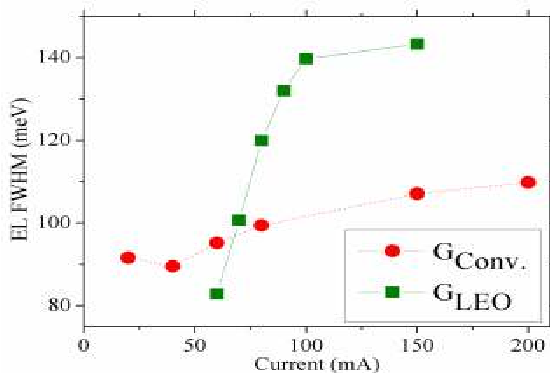

Fig. 30. EL FWHM dependency on current for green LED on conventional (G_{Conv}.) and LEO GaN (G_{LEO}).

electric field built up.

The EL spectra of the green LEDs are shown in Fig. 28. Device G_{LEO} is observed to have longer peak wavelength than device G_{Conv}. (Fig. 28 inset). With increasing current, the EL FWHM increased for both devices (Fig. 29); however, the EL peak-shift of sample G_{LEO} is larger than that of G_{LEO}, possibly due to the effects of piezoelectric fields. These piezoelectric fields may also be responsible for the broader EL FWHM observed in green LEDs. (This could be seen by comparing the ordinates of Fig. 29, and Fig. 30)

Comparing blue and green LEDs, a more pronounced EL peak shift is observed for green LEDs. This suggests stronger piezoelectric effects in the active layer. Piezoelectric effects are expected to be more pronounced in green MQWs due to the higher indium content of the layers. [24] The broader EL-FWHM of green LEDs than those of blue ones indicates a bigger indium fluctuation through the green active layer. [17] This is in agreement with the AFM measurements we have discussed in section II-(a)(Fig. 23, Fig. 24).

The radiant power of the various devices was measured as a function of injection current in continuous wave injection (not shown). Device B_{LEO} achieved 2.6 times more power than B_{Conv}. whereas G_{LEO} and G_{Conv}. had almost the same peak power independent of the template. In near field EL studies of device B_{LEO}, we have observed a stronger luminescence originating from the wing regions compared to the opening regions. This luminescence difference should be related to the density of dislocations on the corresponding regions, demonstrating the role of dislocations as non-radiative recombination centers.[19] For G_{Conv}. and G_{LEO}, we did not observe any difference between luminescence in the wing and opening regions. This supports our reverse bias analysis, and reinforces that the green LED performance is dominated primarily by the active layer quality. In summary, green MQW quality should be improved to reveal the benefits of GaN LEO templates in green LEDs.

D. Conclusion

A five-step LEO GaN growth technique for high quality LEO GaN growth is introduced. Blue and green emitting active layers and LEDs on conventional GaN and five-step-grown LEO GaN templates are realized. AFM, XRD and PL are used to study the structural and optical properties of the active layers, and the effects of dislocations on blue and green active layers are identified. Significant differences in blue and green active layer surfaces are analyzed. The high quality LEO templates are observed to be important for smoother active layer surface morphologies. Blue and green LEDs on conventional GaN and high quality LEO GaN are studied. Green LEDs are observed to be leakier than blue ones, and no significant differences between green LEDs on conventional GaN and LEO GaN in terms of I-V behavior and peak power are observed. Green MQW quality is determined to be the bottleneck for high performance green emitters, not template dislocation density.

V. Green Light Emitting Diodes

A. Introduction

We have performed room temperature photoluminescence (PL) studies on active layers with peak emission wavelengths of 406 nm, 424 nm, 448 nm, 481 nm, 501 nm, 517 nm, 542 nm, 560 nm, and 570 nm as seen in Fig. 31(a). With increasing emission wavelength, a significant decrease in peak emission intensity as shown in Fig. 31(b) is observed. In addition, the longer the emission wavelength the broader the emission spectrum becomes, as seen in Fig. 31(c). The decrease in the

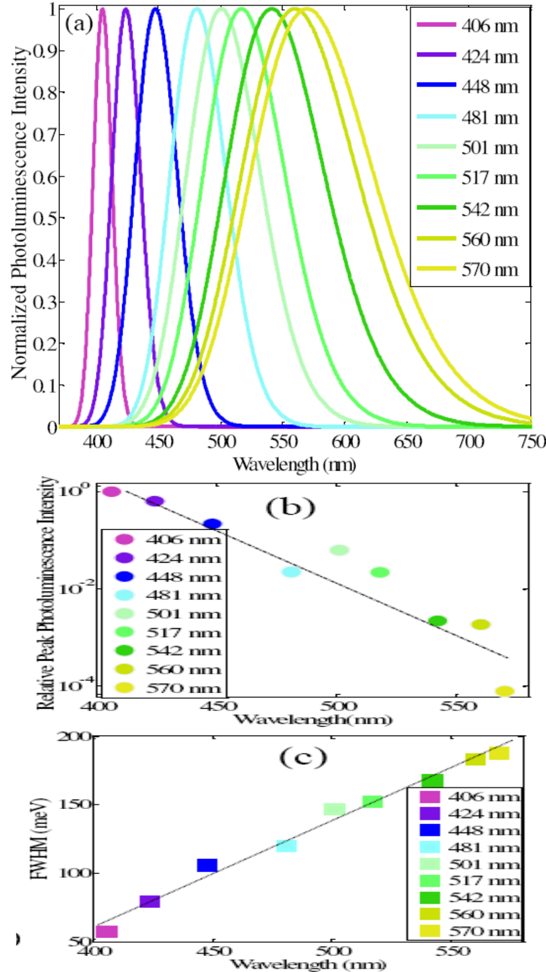

Fig. 31. (a) Normalized Photoluminescence Intensity versus Wavelength at room temperature, (b) Relative Peak PL Intensity (logarithmic scale) versus Wavelength, (c) FWHM versus Wavelength

intensity is related to dislocations generated due to the high indium content InGaN and GaN. The similar intensity decrease is observed even on our high quality LEO samples.

In order to improve the performance of longer wavelength devices we investigate a novel pulsed growth technique. Using pulsed growth can increase the mobility of the adatoms helping them to diffuse till they settle on the correct lattice site. Mobility could be increased by increasing temperature, decreasing the group III element amount, decreasing the pressure. However, increasing temperature and decreasing pressure results in much lower In content in the layers. We have decreased the total group-III amount as feasible as possible, to a growth rate value of 1.18 nm/min. To give the adatoms more mobility, we developed a pulsed layer epitaxy method, without sacrificing emission wavelength, which improved the active layer significantly.

B. Experiment

The pulsed atomic layer epitaxy of InGaN is developed to increase the material quality through increasing the mobility of the adatoms. According to our research, a continuous supply of indium is used whereas gallium is pulsed as indium desorbs from the surface quickly and results a decrease in wavelength.

Table IV

Effect of pulsing time and period on the surface roughness.

T_{In}	T_{Ga}	T_{Total}	No of Periods	AFM Roughness (1μm×1μm)
4	1	4	39	2.68 A
4	2	4	39	3.81 A
4	3	4	39	3.75 A
4	4	4	39	4.42 A
4	1	2	78	3.75 A

In Table 4, the effect of the pulsing time of gallium and pulsing period time is summarized. The active layers are capped with 7 nm GaN. It is seen that with increasing Ga duration time, the surface roughness increases (Fig. 32). In contrast, by decreasing the pulsing period a smoother surface is achieved, as shown in Fig. 33.

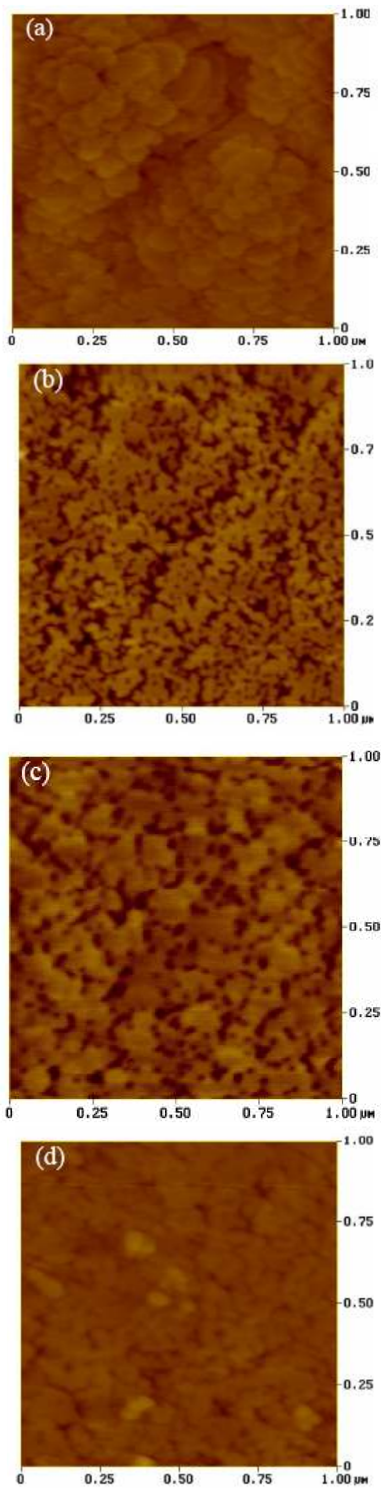

Fig. 32. Effect of Ga pulsing time on surface morphology: (a) 1 sec, (b) 2 sec, (c) 3 sec, and (d) 4 sec.

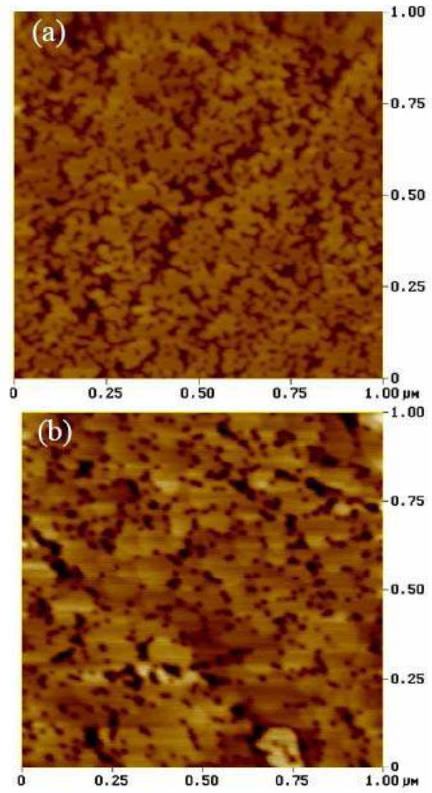

Fig. 33. Effect of one period time on surface morphology: (a) 4 sec total, (b) 2 sec total.

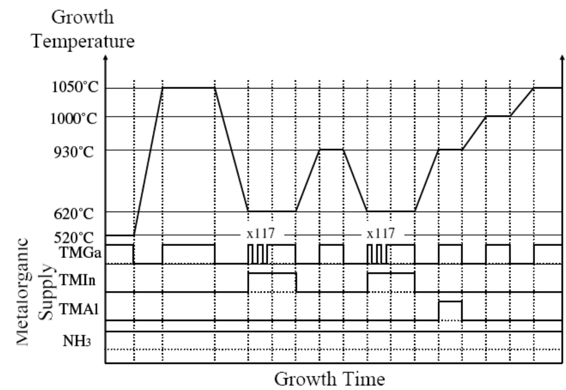

Fig. 34. Growth Temperature and Metalorganic Supply throughout the LED growth

During our research, we have observed that the amount of indium in the active layer is strongly effected by the surface on which active layer is grown. At the same growth temperature, on higher quality GaN, InGaN has a lower indium composition. This also suggests that for multiquantum well growths, as the barrier material is grown at low temperatures and layer quality decrease, the indium content of the resulting active layers increase. This result in a broader emission, and if indium is clustered too much, the failure of light emission. We have resolved this problem by employing a temperature cycling in the active layer (Fig. 34). To achieve a narrower emission, first a low temperature layer thick enough to keep indium inside at barrier growth temperature is grown. After this low temperature layer, higher temperature GaN is grown.

Once the LEDs are grown, activation of the p-type GaN is achieved by rapid thermal annealing (RTA) at 1000℃ for 30 seconds. After surface treatment with HCl:H_20 (1:1), 30 Å Ni / 30 Å Au is deposited as transparent contact and is annealed to achieve ohmic contact to p-type material. ECR-RIE system (using a $SiCl_2$ and Ar chemistry) is then used to etch 300 µm x 300 µm mesas. 400 Å Ti / 1200 Å Au is finally deposited as the thick contact metal for both n- and p-type GaN.

C. *Result and Discussion*

The devices have a turn on voltage of 6.2 V with turn-on resistance ~90 Ω (Fig. 35). The electroluminescence spectrum is shown in Fig. 36.

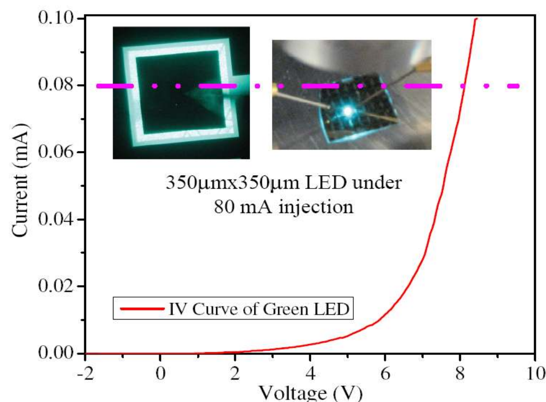

Fig. 35. Current Voltage characteristics of a green LED. Inset pictures display a 300 µm × 300 µm LED under 80 mA current injection.

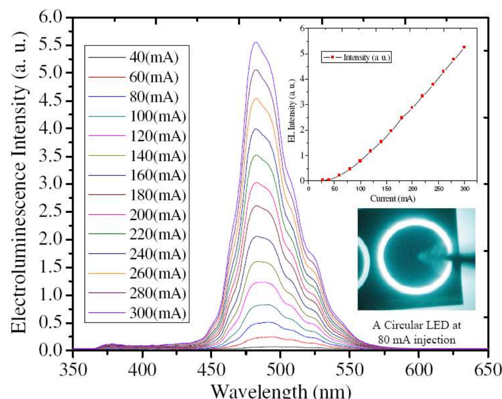

Fig. 36. Current Dependent Electroluminescence of the Green LED. Inset displays the current dependence of the peak intensity.

D. *Conclusion*

The active layer quality is improved by using pulsed atomic layer epitaxy for InGaN. Thermal cycling in the active layer is developed to ensure uniformity and quality of the quantum wells. We have demonstrated green LEDs with emission wavelength 510 nm at 20 mA. A blue shift with injection current similar to blue LEDs are observed.

E. *Future Work*

In future work, we plan to integrate aluminum inside the barriers to help ensure higher indium contents in the well layers are preserved. This should also lead to a higher device performance due to better confinement. The drawback is the strain-related blue shift in the active layer emission. We will prepare high quality LEO GaN substrates to study the effect of these substrates on green light emitting diodes.

VI. Novel Hybrid Green LEDs Based on Substituting n-type ZnO for n-type GaN in an Inverted p-n Junction

A. *Introduction*

Solid state lighting (SSL) holds the promise of a more energy-efficient, longer-lasting, more compact, and lower maintenance substitute for today's incandescent and fluorescent light sources. Since lighting currently represents about 22% of all electricity consumption, the adoption of SSL could significantly reduce greenhouse gas emissions. [11] Light-emitting diodes (LEDs) based on the InGaN alloy, are currently the most promising candidates for realizing SSL. InGaN is a direct wide bandgap semiconductor with an emission which can span the entire visible spectrum via compositional tuning. InGaN LED performance remains wavelength-dependent, however. Indeed, ultra-bright and efficient blue InGaN-based LEDs are readily available [12] but the performance of InGaN-based green LEDs is still far from adequate for use in SSL. [13], [14]

The higher In content required in the active layers for green emission causes problems. Firstly, the limited solubility of In in GaN [20] imposes a restricted growth window for the green-emitting InGaN active layer. Secondly, InGaN with high In content becomes unstable at elevated substrate temperature (Ts). [21] Conventionally, a p-GaN layer is grown on top of an InGaN multi-quantum-well (MQW) active layer. The p-GaN layer is grown at significantly higher Ts than the InGaN MQW active layer in order to obtain high structural quality. This leads, however, to In leaking out of the active layers, which reduces the LED output.[14] Thus, it is important to combat In diffusion in order to obtain InGaN based green LEDs with superior performance.

ZnO is a wide bandgap material (Eg=3.3 eV) with a large exciton binding energy (60 meV). It has a low toxicity and the same wurtzite structure as GaN. The small in-plane lattice mismatch (~1.8%) with GaN makes ZnO a good candidate for integration in nitride devices. [6], [47] Recently, there have been many reports of ultraviolet emitters based on n-ZnO/p-GaN heterostructures. [5], [48], [49] In this work,

ZnO is adopted as the n-layer in a new kind of hybrid green LED. [15]

In conventional GaN-based LEDs, the p-layer is deposited on top of the n-layer, because the n-layer can be grown with higher crystallographic and morphological quality than the p-layer. In this work, we adopted an inverted LED structure employing an n-ZnO layer grown on top of (In)GaN MQW/p-GaN/AlN/Sapphire. Through the use of pulsed laser deposition (PLD), a high quality n-ZnO layer could be grown at significantly lower Ts than is typically required for GaN growth in metalorganic chemical vapor deposition (MOCVD). This approach could be beneficial, particularly for green light emitters, in which, the high In content InGaN active layers are adversely affected by the high Ts required for the GaN growth. Furthermore, the refractive index of ZnO at 500 nm is 2.0 compared with 2.5 for GaN. Thus, lower critical angle loss is expected for light extraction through ZnO-capped LEDs.

In this chapter, we explain the fabrication of these hybrid LEDs, and investigate the optical, structural, and electrical characteristics of the fabricated devices.

B. Experiment

The AlGaInN compounds were grown in an AIXTRON 200/4-HT horizontal flow, low pressure MOCVD reactor. Trimethlyaluminum (TMAl), Trimethylgallium (TMGa), Trimethlyindium (TMIn), and Bis(cyclopentadienyl)-magnesium (DCpMg) were the metalorganic cation precursors for Al, Ga, In, and Mg sources, respectively. Ammonia (NH_3) was used as the nitrogen source. Hydrogen was used as the carrier gas in the AlN and p-GaN layers.

First, a 600 nm-thick AlN layer was grown on the c-sapphire in order to improve the quality of the subsequent p-GaN layer. [50] Rapid thermal annealing was realized at 1000°C for 30 seconds in order to activate the Mg dopant. Then, a five period multi-quantum well structure was grown in a nitrogen ambient. Each period consisted of a 2-nm-thick InGaN quantum-well with a 4-nm-thick GaN barrier. An n-ZnO layer was grown on top of the (InGaN/GaN) MQW/p-GaN using PLD of a sintered ZnO target with a KrF (248nm) excimer laser. A ZnO layer was also simultaneously grown directly on c-sapphire as a reference for characterization studies.

C. Result and Discussion

First the structural, electrical and optical properties of hybrid LED layers were reported, and then the effects of solvents, annealing and etching on n-ZnO were shown. Thanks to these studies, integration of ZnO in (In)GaN based green LEDs was realized.

1) Structural characterization of the layers

Scanning Electron Microscopy (SEM) was performed in a Hitachi S4500 microscope equipped with an Oxford Energy Dispersive X-ray microanalysis (EDX) system and Atomic Force Microscopy (AFM) was conducted using a Veeco Dimension 3100 Scanning Probe system.

SEM images of the ZnO reference sample surface revealed a relatively featureless morphology (Fig. 37 (a)), free of the particulates or droplets, which can be an issue with PLD growth. Tapping mode AFM gave root mean square (RMS) roughnesses of 5.6 Å and 4.7 Å for (3 μm×3 μm) and (1 μm×1 μm) scans, which are shown in Fig. 37 (b) and (c), respectively.

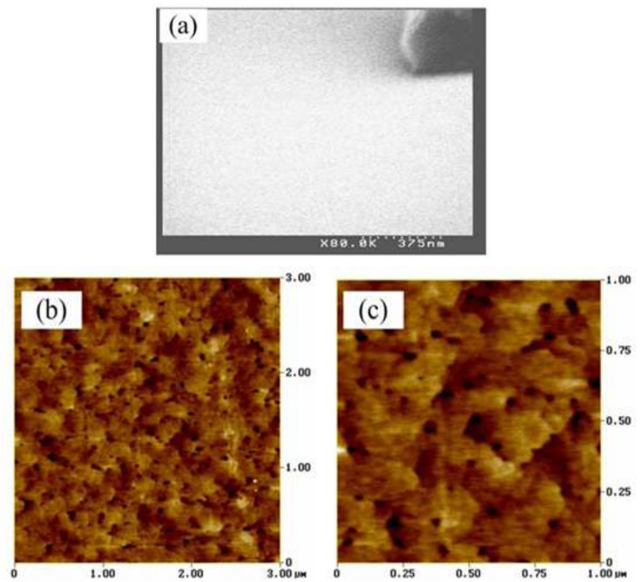

Fig. 37. (a) SEM surface micrograph, (b) AFM scan (3 μm ×3 μm), (c) AFM scan (1 μm ×1 μm) of the surface of n-ZnO/Sapphire.

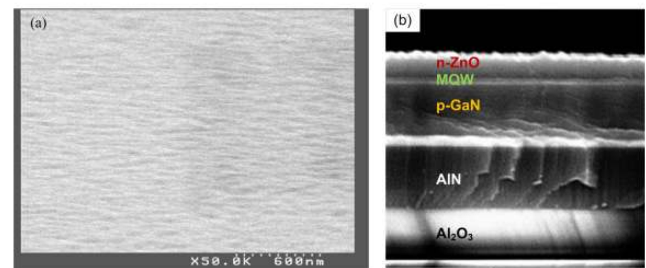

Fig. 38. SEM micrographs of the hybrid LED: (a) Surface and (b) Cross-sectional view.

Fig. 38 (a) shows an SEM micrograph of the top surface of the n-ZnO layer of the fabricated hybrid LED. The surface morphology appears slightly rougher than the as-grown n-ZnO on sapphire (Fig. 37 (a)). Fig. 38(b) shows an SEM fracture

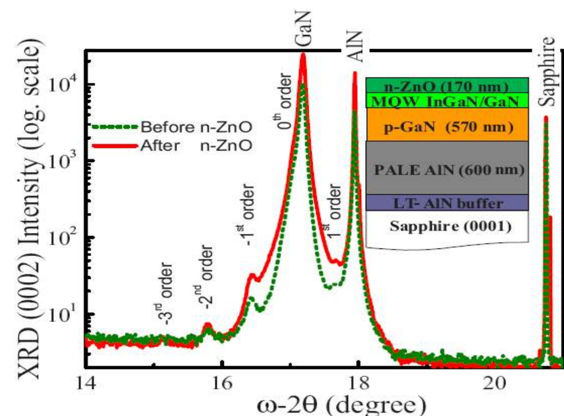

Fig. 39. RT XRD ω/2θ scans for the (0002) peak before- and after- growth of *n*-ZnO on the (InGaN/GaN) MQW/*p*-GaN/AlN/Sapphire.

cross-sectional image. The n-ZnO / MQW/ p-GaN/ AlN/ Sapphire (Al_2O_3) LED layers can clearly be distinguished.

X-ray diffraction (XRD) studies were performed using a High Resolution Panalytical MPD-Pro system Diffractrometer. ω-2θ scans for the (0002) peak of the LED structure are shown in Fig. 39. The ZnO and GaN peaks are indistinguishable, suggesting a good lattice match. The MQW-related, satellite peaks are similar before and after the ZnO growth. This indicates that the active layers maintained their compositional and structural integrity

2) Electrical characterization of the layers

Room temperature Hall effect measurements were performed on the *n*-ZnO/Sapphirein Van der Pauw configuration (with a magnetic field strength of 0.3 T) with 400Å Ti/300Å Pt/1200Å Au contacts. The *n*-contacts proved ohmic and carrier concentration was determined to be 2.8×10^{19} cm^{-3} with a mobility of 10.0 $cm^2/V\cdot s$, and a resistivity of 0.02Ω ·cm. Similarly, hole carrier concentration for the p-GaN was determined to be $7.8\times10^{17} cm^{-3}$ and 30Å Ni / 30Å Au transparent p-contacts were observed to be ohmic.

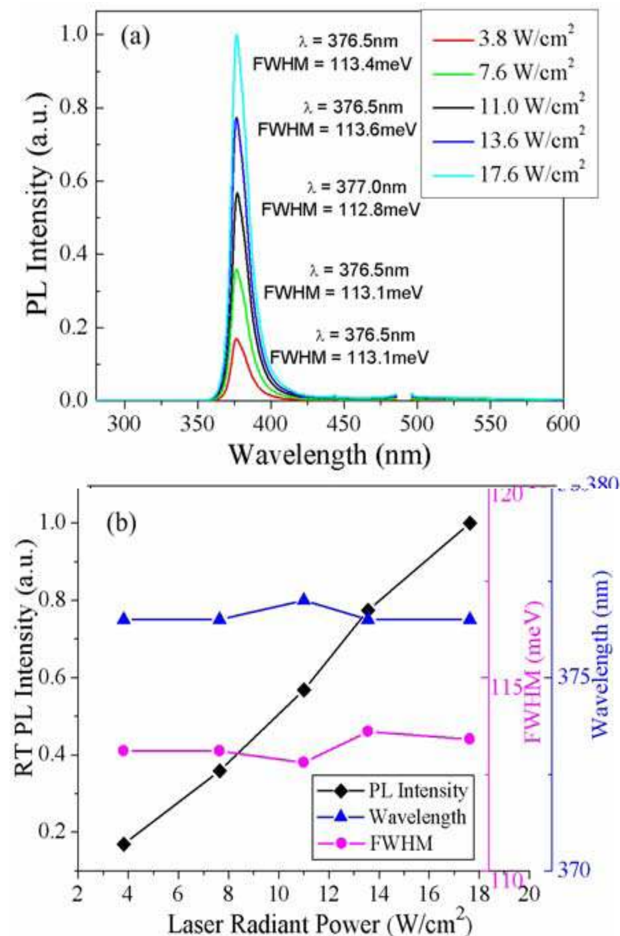

Fig. 40. (a) RT PL spectra at different laser powers for *n*-ZnO/sapphire, (b) Peak PL intensity, PL FWHM and wavelength dependency on radiant laser power for *n*-ZnO/sapphire.

3) Optical characterization of the layers

Photoluminescence (PL) measurements were carried out at RT with a frequency-doubled argon-ion laser at 244 nm. Room temperature PL for the n-ZnO/sapphire reference sample revealed a single peak at 377 nm corresponding to the n-ZnO band-edge. The spectrum also had relatively low green signal, which implies that there is a relatively low defect/dislocation density in the sample. Laser power dependent measurements showed no significant peak shift or full-width-at-half-maximum (FWHM) broadening (Fig. 40(a, b)). A linear increase in PL main peak intensity with increasing laser radiant power was observed. These results indicate high optical quality of the ZnO layer.

Normalized RT PL spectra for the hybrid device are shown in Fig. 41. The spectrum for the p-GaN is dominated by a 426 nm Mg-related peak, which was attributed to defect-related deep level centers. [51] The PL spectrum, once the InGaN/GaN MQWs were grown on the p-GaN, shows a strong emission peaked at 496 nm without the 426 nm Mgrelated peak. The PL spectrum for the completed hybrid LED structure (including the n-ZnO top layer) shows the strongest main emission peak, centered at 376 nm, corresponding to the ZnO band-edge and is similar to the PL observed for the ZnO/sapphire reference sample.

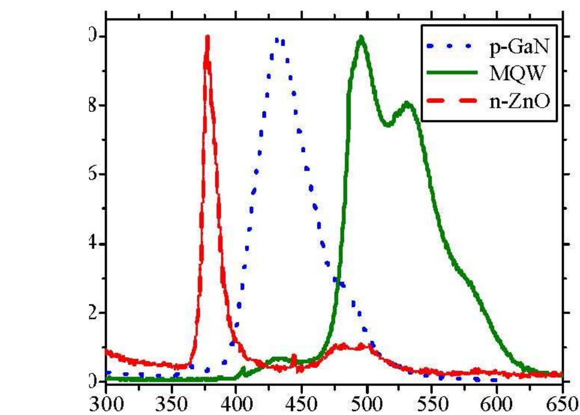

Fig. 41. RT normalized PL spectra as consecutive p-GaN, InGaN/GaN MQW, and n-ZnO layers were grown on AlN/Sapphire.

4) Effects of common solvents on ZnO

The effect on ZnO of the common solvents used in the fabrication of the InGaN LEDs (deionized (DI) water, acetone, trichloroethylene (TCE), methanol and stripper) was studied. After each step, SEM was used to investigate any potential impact on the n-ZnO surface. Fig. 42 displays SEM micrographs of the initial ZnO surface (a) and the surface after consecutive immersion in (b) DI water, (c) acetone, (d) TCE, (e) methanol, and (f) stripper. No significant degradation of the n-ZnO surface was observed after treatment with these solvents.

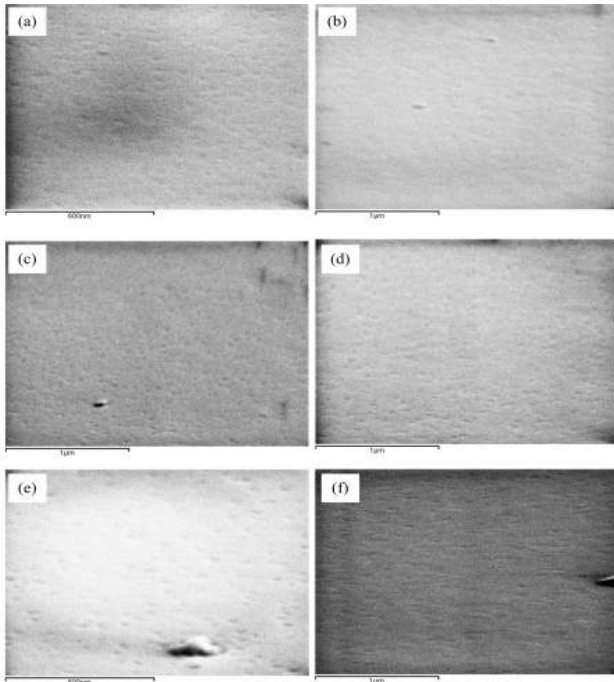

Fig. 42. SEM micrographs of (a) the initial n-ZnO surface and after treated with (b) DI water, (c) acetone, (d) TCE, (e) methanol, and (f) stripper, consecutively.

D. *Effect of annealing*

Annealing is a crucial parameter in order to obtain low resistance ohmic contacts to p-GaN. Our studies established that 30Å Ni/ 30 Å Au contact to p-GaN was least resistive when annealed at 500ºC for 10 mins in air. Thus, an annealing test of the n-ZnO layer was realized under this condition. This annealing was determined to damage the n-ZnO surface. Thus, p-contacts were not annealed for these hybrid LEDs. Evaporated 30Å Ni / 30Å Au / 400Å Ti / 1200Å Au were found to be ohmic, however. Further studies are being carried on for optimization of annealing with regard to overall LED performance.

E. *Etching study*

Dry etching was preferred to wet-etching for consistency and for the realization of better side-wall profiles. A systematic study of dry etching (with a Plasmatherm electron cyclotron resonance reactive ion etching (ECR-RIE) system) was conducted. For the GaN, a ($SiCl_4$ + Ar) chemistry was adopted based on our prior studies. For the n-ZnO, (CH_4 + Ar) chemistry was employed, with Ar at 5 mTorr. A common side-wall angle of ~70º was observed (Fig. 43). The n-ZnO etch rate was determined to be 53 nm/min.

X-ray microanalysis gives information about the elemental composition of the specimen, in terms of both quantity and distribution. An etch-test EDX study shown in Fig. 44 indicated that etched layers of n-ZnO had a lower Zn atom density than the as-grown layer. Al and O atom densities were also observed to be higher on the etched surface relative to those on the as-grown mesa area. Fig. 44 (b, c) gives the normalized scale for the EDX count rates for Zn, Al and O atoms for the etched and as-grown layers showing the spatial distribution of elements.

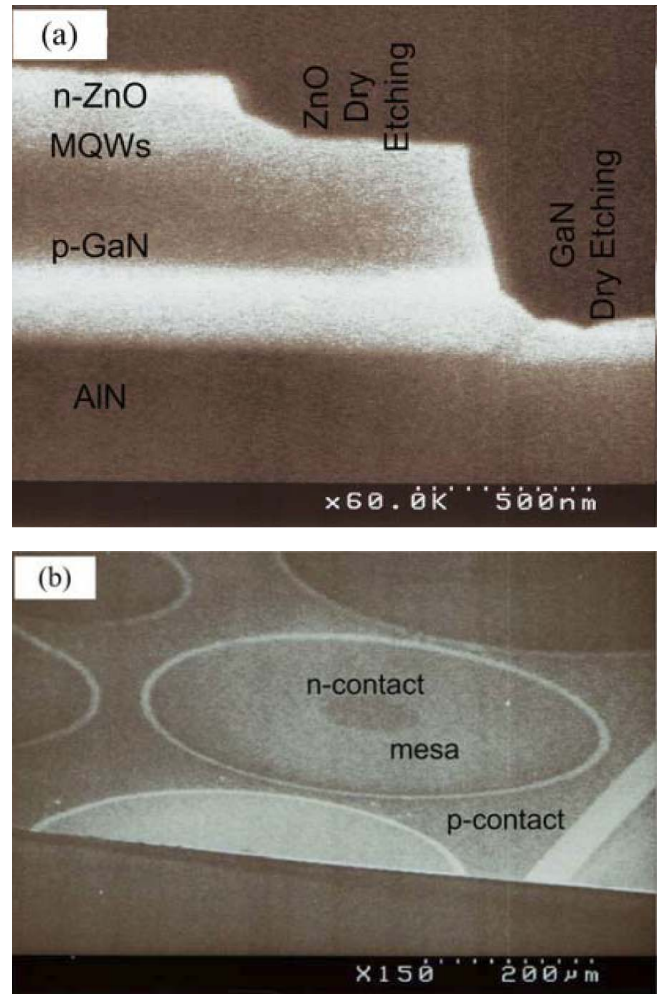

Fig. 43. SEM micrographs of a fabricated hybrid LED (a) Side view, (b) Top (angled) view

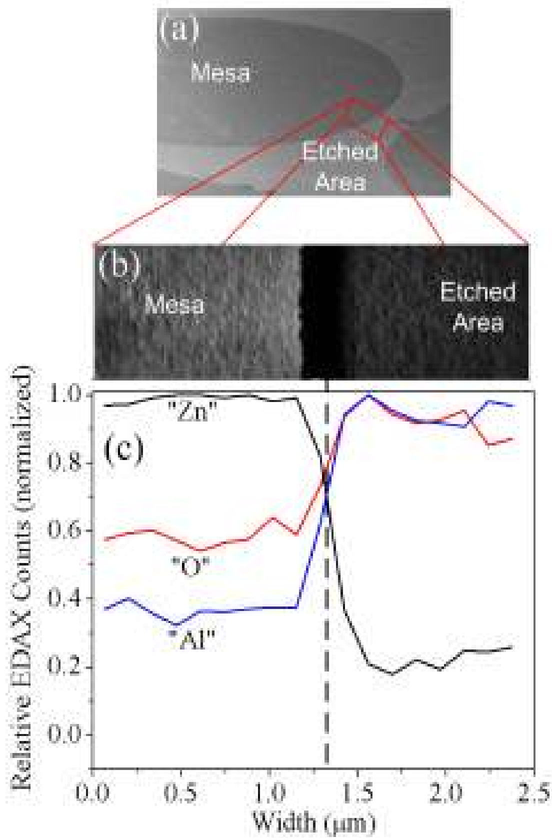

Fig. 44. (a) Dry etching of *n*-ZnO on sapphire, (b,c) EDX system analysis shows the relative concentrations of O, Al and Zn atoms through 2.46 μm (from mesa through etched area). The EDX scale is normalized and relative.

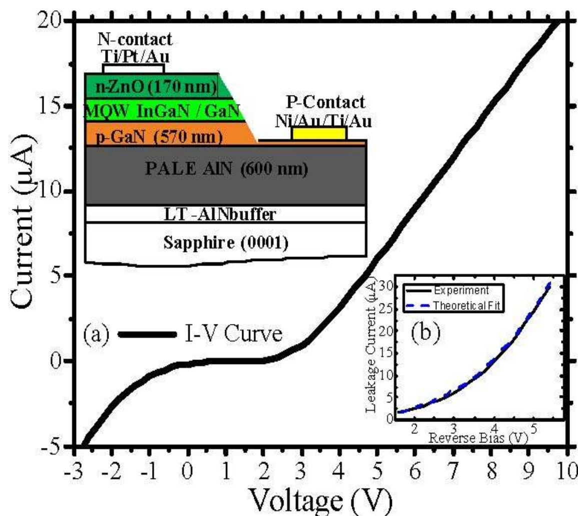

Fig. 45. (a) I-V Curve of the fabricated LED. The device structure is illustrated in the inset. (b) Leakage current versus reverse bias voltage: Experimental and theoretical fit for the reverse-bias voltage range -1.6 to -5.4 V.

F. Device performance

After optimization of the fabrication process, hybrid green LEDs were fabricated using optimized processing techniques. First of all, the samples were cleaned chemically. The cleaning steps included TCE, acetone, methanol treatment and rinsing. Circular LED mesas, with an area of 0.30 mm^2, were fabricated by masking the surface and dry etching right through the n-ZnO layer to a depth of 500 nm into the p-GaN.

Fig. 45(a) shows a typical I-V curve for a green emitting hybrid LED. The turn-on voltage is around 2.5 V, which is close to the bandgap energy observed in the PL spectrum (Fig. 41). The on-series resistance (R_S) is calculated via a linear fit to the equation [52] I dV/dI = R_SI+ kT/e for V >> kT/e, and determined to be 4.75 MΩ. This relatively high value is most likely due to (1) high contact resistance because the metal contacts to the *p*-GaN were not annealed, and (2) the closeness (~70 nm) of the *p*-contact to GaN/AlN interface, which could lead to interface effects such as a 2-D electron gas or elevated dislocation densities corrupting the ohmic nature of the contact. Rs could be lowered through use of a lower *p*-GaN etch depth to increase the separation between the contact and GaN/AlN interface. The Ni/Au was not annealed to make a better ohmic contact with the *p*-GaN because the ZnO surface morphology was observed to be modified by annealing at 500ºC. Decreasing the *p*-GaN etch depth and annealing the *p*-contact could improve the forward-bias (FB) I-V characteristics. Under FB, green light was easily observed with the naked eye at RT under continuous-wave (CW) operation.

Reverse-bias characteristics are zoomed in Fig. 45(b). As the *p*-GaN contact is close to the GaN/AlN interface, where there are many dislocations, a highly non-linear increase in leakage current with respect to reverse bias voltage was observed. The leakage current is known to be proportional to the square of the density of dislocations. [29] At high reverse bias, there is field-assisted thermal ionization of carriers from the defect-associated traps, which is known as Poole-Frenkel effect. Thus, the leakage current is expected to obey [43], [45]

$$I = I_0 \exp\left(\frac{\beta_{BF} E^{1/2}}{kT}\right), \qquad (2)$$

The average electric field (E) dependence on the reverse bias (V) was found from E = (V + V_i)/w, where V_i is the built-in junction voltage, and w is the depletion width. [45], [53] Fig. 44(b) plots the best fit of Eqn. 2 to our experimental data. From this fit, we obtain $ß_{BF}$ =7.6×10^{-4} eV $V^{1/2}$ $cm^{1/2}$. This value is slightly higher than that for GaN (4.5×10^{-4} eV $V^{1/2}$ $cm^{1/2}$).[43] For higher density of dislocations, $ß_{BF}$ tends to be bigger [29], [43], [45]. Since leakage current scales with the square of the density of dislocations [29], the effective density of dislocations was calculated to be 8.2×10^{-8} cm^{-2}. This theoretical fit shows that under reverse bias, hopping conduction is dominant in these hybrid LEDs similar to conventional p-n

(In)GaN diodes. [43], [45] Further optimization of the hybrid LED design and fabrication process are in progress.

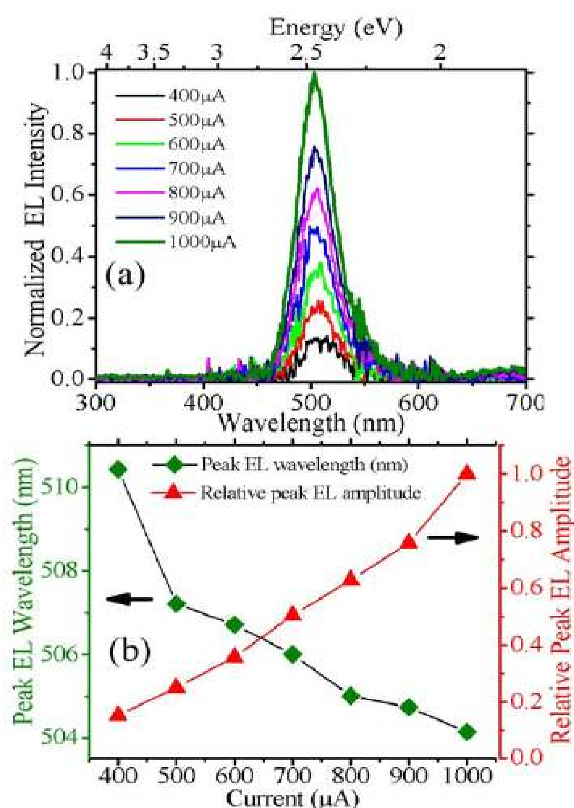

Fig. 46. (a) Normalized electroluminescence (EL) intensity of the hybrid green LED at room temperature, (b) Peak EL wavelength and amplitude with respect to injection current.

Output power of the hybrid LED was measured utilizing a calibrated integrated sphere. Under forward bias, green light was easily observed with the naked eye at RT under continuous-wave (CW) operation. Optical output power was on the order of µW. Electroluminescence spectra were acquired under pulsed operation (duty cycle of 10%, frequency = 5 kHz) in order to reduce heating effects under higher current injection. EL spectra (Fig. 46) revealed an emission peaked in the green regime with a blueshift from 510 nm to 504 nm as the current increased from 400 µA to 1000 µA. The FWHM decreased simultaneously from 194 meV to 179 meV. These effects were attributed to free-carrier screening of the piezoelectric field, which led to bandgap renormalization.[54] The spectral narrowing for the device demonstrated no band-filling effects, even for higher current injections, and thus indicated superior quality of the active layer [25]. This was consistent with the high compositional and structural integrity of the MQWs inferred from the XRD studies (Fig. 39) and can be attributed to the lower Ts employed for PLD of the ZnO top n-layer. More device details can be found in refs. [15], [55].

Further optimization of the hybrid LED design and fabrication process are in progress, including improvement of electron and hole current spreading through adjustment of the n-ZnO and p-GaN layer thicknesses. p-GaN etch-depth is also under investigation, in order to inject holes more uniformly. Thicker green active layers are also being developed, which should give higher output in the green (since the ZnO growth temperature is lower than that for the InGaN, thicker InGaN layers should be more stable).

G. *Conclusion*

Novel hybrid green LEDs were developed. These devices employed an inverted p-n structure and the substitution of n-ZnO for the n-GaN layer. Conventional MOCVD growth was used for the p-GaN and MQWs. Lower temperature PLD was adopted for the ZnO growth in order to combat thermal degradation of the InGaN layers. High structural and optical quality of the ZnO, GaN and (In)GaN layers were confirmed using XRD and PL analyses, which suggested that the integrity of the MQW was maintained.

The effects of common solvents, etchants and annealing on n-ZnO were investigated. No significant degradation of the n-ZnO surface was observed after consecutive treatment with DI water, acetone, TCE, methanol, and stripper. Dry etching of n-ZnO with (CH_4 + Ar) chemistry was found to give good side-wall profiles for the device fabrication. Some minor degradation of the n-ZnO surface was observed after the 10-minute anneal at 500°C in air, which is commonly adopted for p-GaN transparent contact optimization. Evaporated 30Å Ni / 30Å Au / 400Å Ti / 1200Å Au and 400Å Ti / 300Å Pt / 1200Å Au contacts were found to give ohmic contacts to the p-GaN and n-ZnO, respectively, without annealing.

Under these processing conditions, a hybrid LED giving green EL between 510 and 504 nm, with a CW output on the order of µW, at RT was realized. Such an inverted hybrid structure approach could hold the prospect for the development of future green LEDs with superior performance.

VII. STRANSKI-KRASTANOV GROWTH OF INGAN QUANTUM DOTS EMITTING IN GREEN SPECTRA

Self-assembled InGaN quantum dots (QDs) were grown on GaN templates by metalorganic chemical vapor deposition. 2D–3D growth mode transition through Stranski– Krastanov mode was observed via atomic force microscopy.[56] The critical thickness for $In_{0.67}Ga_{0.33}N$ QDs was determined to be four monolayers. The effects of growth temperature, deposition thickness, and V/III ratio on QD formation were examined. The capping of InGaN QDs with GaN was analyzed. Optimized InGaN quantum dots emitted in green spectra at room temperature.

A. *Introduction*

Solid state lighting (SSL) holds the promise of a more energy-efficient, longer-lasting, more compact, and lower maintenance substitute for today's incandescent and fluorescent light sources. Since lighting currently represents about 22% of all electricity consumption, the adoption of SSL could significantly reduce greenhouse gas emissions.[11] Light-emitting diodes (LEDs) based on the InGaN alloy are

currently the most promising candidates for realizing SSL. InGaN is a direct wide-band-gap semiconductor with an emission that can span the entire visible spectra via compositional tuning.

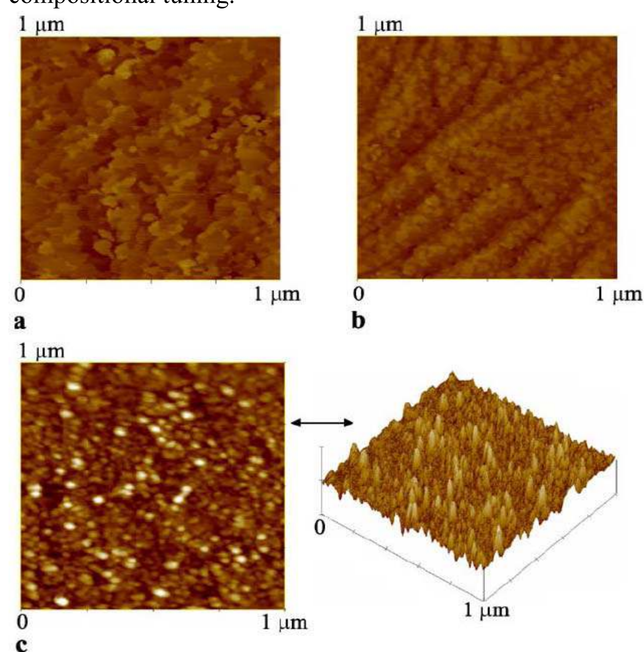

Fig. 47. AFM (1 μm × 1 μm) images of 5.8 ML InGaN grown at (a) T = 734ºC, (b) T = 679ºC, and (c) T = 633ºC.

With increasing indium content (from violet to green emission) a significant decrease in performance is observed in light emitters based on quantum wells [13], [15]. One of the crucial reasons is that the large lattice mismatch between high indium content InGaN and GaN induces the generation of dislocations in the active region [13], [31], [57] This explains how the performance decreases for high indium content light emitters, even on low-dislocated templates [31], [58]. The use of quantum dots may be one way to overcome these limitations in high-indium-content devices. Strain due to high indium content can be channeled into quantum dot (QD) formation which can decrease the overall strain otherwise which would form dislocations [59]. Besides, optoelectronic devices based on QDs have many advantages over those based on QWs, such as temperature stability and higher efficiency [60].

Room temperature blue emission from QDs was reported earlier [61], [62]. The strong luminescence from these QDs was attributed to the exitonic transitions [63]. The blue QDs have been integrated into LEDs [64]. However, there are few studies of InGaN quantum dots in the green spectra [65]. In this work, we study the formation of high-indium-content InGaN QDs, and study the effect of growth temperature, deposition thickness and V/III ratio on QD formation. We also report the stability of GaN capped InGaN QDs grown by Stranski–Krastanov (SK) mode.

B. *Experiment*

The samples are grown in an AIXTRON 200/4-HT horizontal flow, low-pressure metalorganic chemical vapor deposition (MOCVD) reactor. Trimethylgallium (TMGa) and trimethlyindium (TMIn) are the metalorganic cation precursors for Ga and In sources, respectively. Ammonia (NH_3) is used as the nitrogen source. All QD growths are realized under N_2 to facilitate the incorporation of indium.

The InGaN layers were grown on 2-μm-thick GaN on double side polished (DSP) (0001) sapphire (Al_2O_3) substrate. The growth rate was 11.8 Å/min and growth was interrupted for 15 s under ammonia before cool down. We studied the effect of temperature, deposition thickness, and V/III ratio on the formation and optical quality of the InGaN QDs.

C. *Result and discussion*

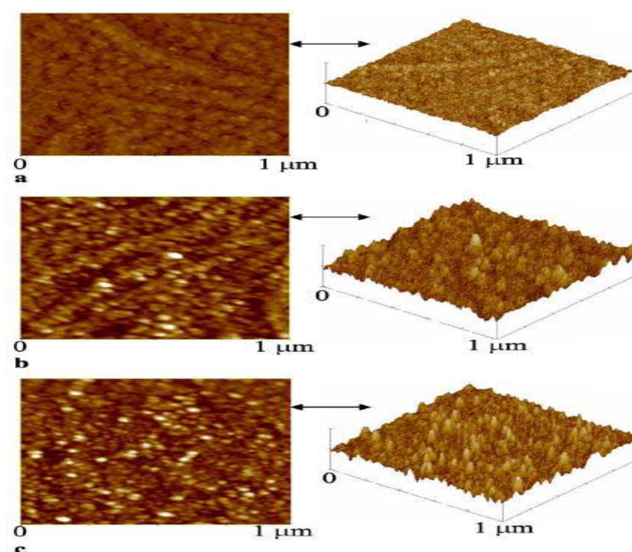

Fig. 48. AFM (1 μm × 1 μm) images of (a) 2.9 ML, (b) 4.4 ML, and (c) 5.8 ML InGaN grown at T=633ºC.

Atomic force microscopy (AFM) was used to study the QD formation. Fig. 47 (a, b, c) displays the (1 μm × 1 μm) AFM images of 5.8 monolayer (ML) InGaN grown at 734°C, 679°C, and 633°C, respectively (1 ML ≈ 2.7 Å). At 734°C, as seen in Fig. 47(a), only island like 2-D quantum disks (Q-disks) formed. Lowering the growth temperature (Ts) further resulted in smaller disks and surface roughening (Fig. 47 (b)). This behavior was attributed to the decrease in adatom mobility and increase in the indium content of Q-disks. The adatom mobility decreased as a result of lowered Ts, and indium content increased due to higher indium thermodynamic equilibrium at low temperatures. Effecting both the thermodynamic (indium content in InGaN) and kinetic (mobility) equilibrium on the surface, temperature is observed to be the most crucial parameter of high-quality QD growths. We have determined 633°C to be a proper growth temperature for green emitting InGaN QDs.

Fig. 48 (a, b, c) displays the (1 μm ×1 μm) AFM images of 2.9-, 4.4-, and 5.8-ML-thick InGaN grown at 633°C, respectively. At this Ts, critical thickness for QD formation is determined to be ~4.0 ML. Below the critical thickness, no QDs are observed (and the surface is similar to Fig. 48 (a)). Above critical thickness, increasing the deposited InGaN results in increase in the density of the QDs in the expense of uniformity (Fig. 48(b, c)).

The effect of V/III ratio on the surface morphology is studied. Fig. 49 displays the AFM root-mean-square (RMS) roughness

(1 μm × 1 μm) of 4.0 ML InGaN layer with respect to V/III ratio at Ts of 633°C. For this deposition thickness and temperature no QDs are observed. As seen in Fig. 49, V/III ratio strongly effects the surface roughness. We have determined 13.88×10^3, where the roughness is maximized in Fig. 49, to be a proper V/III ratio for QD formation at 633°C.

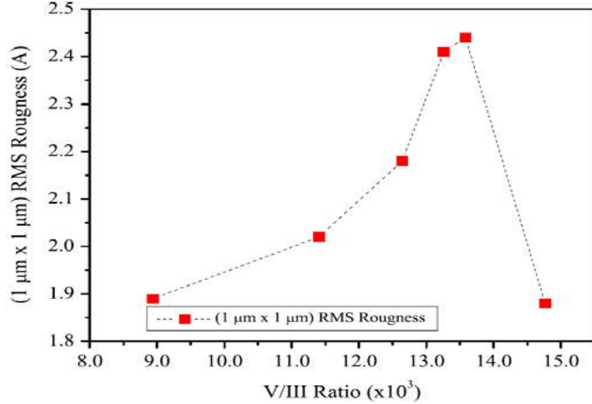

Fig. 49. AFM RMS roughness (1 μm × 1 μm) versus V/III ratio for 4.0 ML InGaN grown at T=633ºC.

Effect of V/III ratio on QD formation is studied separately. Fig. 50 (a, b) displays the (1 μm × 1 μm) AFM images of 5.8-ML-thick InGaN grown at 633°C with V/III ratio being 13.88×10^3 and 13.57×10^3, respectively. As seen, higher V/III ratio results in bigger quantum dots, similar to increased RMS roughness in Fig. 49. V/III ratio being 13.88×10^3, increasing or decreasing V/III ratio results in less uniform quantum dots. Thus, we have kept the V/III ratio at 13.88×10^3 thereafter.

Maintaining the growth temperature at 633°C, and V/III ratio at 13.88×10^3, we have identified formation of two different quantum structures: quantum disks and quantum dots. When InGaN is deposited less than critical thickness of 4 ML, some kind of 2-D structure similar to Fig. 48 (a) was observed. As the height of these structures were much smaller than their width (as observed via AFM analyses), they are referred to as quantum disks. Deposited more than 4 ML, QD formation was observed via AFM (Fig. 48 (b, c)).

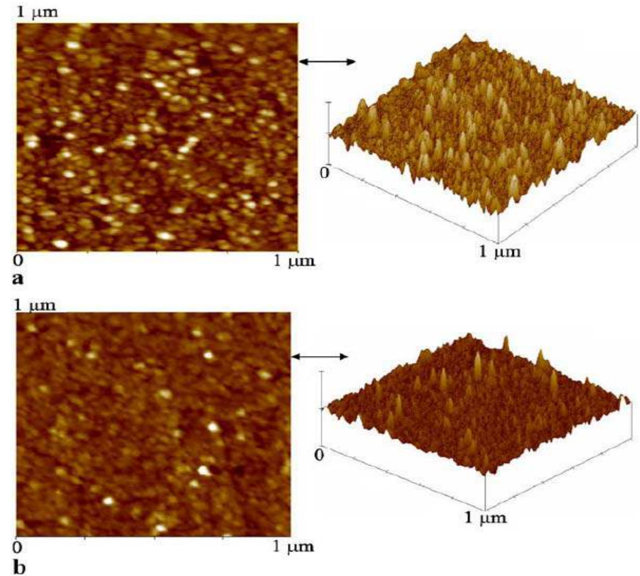

Fig. 50. AFM (1 μm × 1 μm) images of 5.8 ML InGaN grown at T=633ºC with a V/III ratio (a) 13.88×10^3, and (b) 13.57×10^3.

The photoluminescence of the InGaN quantum structures were studied at room temperature (Fig. 51) via 244 nm line of Argon laser. Due to low excitation (18 W/cm^2), the main transition in QDs is from ground levels of conduction and valance bands. Fabry–Perot reflections (in Fig. 51) are observed due to 2-μm-thick GaN cavity. At 558 nm calculated Fabry–Perot peak separation is 34 nm not far from what we experimentally observe.

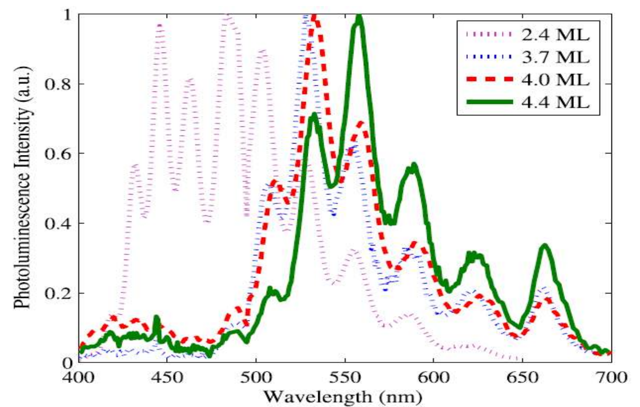

Fig. 51. Normalized photoluminescence intensity versus wavelength at room temperature for 2.4-, 3.7-, 4.0-, and 4.4-ML-thick InGaN.

At our optimized growth conditions, InGaN relaxes into two different quantum structures, quantum disks or quantum dots depending on the deposited thickness. For ~2.4ML InGaN deposition, the layer is pseudomorphic, and broad band emission from 420 to 520 nm is observed. For InGaN deposition ≥3 ML, the layer tends to partially relax by forming quantum disks, as shown in Fig. 48 (a), which leads to two distinct PL bands in Fig. 51. The first band (420–460 nm) presenting a low PL emission intensity is attributed to a wetting layer. The existence of this wetting layer is due to SK mode. The high-intensity band has a peak at 525 nm and corresponds to emission from the (higher indium content) quantum disks. At a thickness of 4.4 ML, quantum dot formation occurs, as shown

in Fig. 48 (b). Two PL bands are also observed, but the high-indium-content band corresponding to QD emission has a longer wavelength (558 nm) than that of the quantum disk. In conclusion, QD formation takes place after deposition of critical thickness of about 4.0 ML with an apparent PL redshift. When 4.4 ML InGaN is deposited, the average size of the quantum dots are 0.8 nm in height and 36 nm in bottom diameter, and their density is 1×10^{10} cm^{-2}.

In Ref. [66], the detrimental effect of quantum dot height on radiative lifetime is reported. The strong room temperature luminescence of our QDs should be due to smaller QD height leading to a higher overlap between electron and hole wavefunctions. Thus, achieving high-optical-quality InGaN QDs requires precise control of the InGaN growth rate and is attainable at low growth rates via MOCVD.

Integrating the QDs in LEDs requires an appropriate means of capping. A low-temperature GaN capping layer is investigated to cap 4.4 ML InGaN QDs. For a 2-nm-thick capping layer we can still resolve the QDs by AFM (Fig. 52 (a)). However, with 5-nmthick capping, the QDs are completely covered (Fig. 52 (b)). The PL intensity dependence on capping thickness is shown in Fig. 52 (c). When just covered, the PL intensity increases. However, a thicker capping layer reduces the emission intensity possibly due to the absorption losses in the thick GaN capping layer.

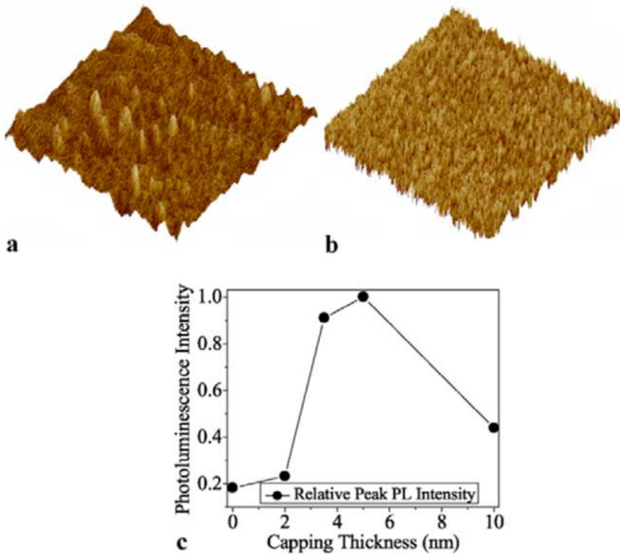

Fig. 52. AFM Surface Plot for (a) 2 nm capped (1 µm ×1 µm), (b) 5 nm capped (5 µm ×5 µm) 4.4 ML InGaN QDs. (c) Peak photoluminescence intensity dependence on capping thickness.

D. Calculation of indium content

Iterative calculation of strain and piezoelectric effects on the band gap are used along with ground energy levels to estimate the indium content of the InGaN QDs using experimental PL data as input. The set of parameters used in this work could be found in Ref. [67]. Vegard's Law is used to interpolate values for $In_xGa_{(1-x)}N$.

The InGaN QDs are known to have trapezoidal shape, which can be observed via transmission electron microscope studies [68]. Thus, InGaN QDs are assumed to have a trapezoidal shape with 35° side wall angle while calculating the ground state energies by finite-element modeling (FEM). The relation between band gap determined from PL (E_g^{PL}) and real compositional band gap (E_g^x) is approximated as follows:

$$E_g^{PL} = E_g^x + E_x^{g-g} + \Delta E_g \qquad (3)$$

where strain and piezoelectric field effects are included in ΔE_g . E_x^{g-g} is the sum of the conduction and valance band ground energy levels relative to their respective bands. Finite-element modeling is used to calculate the ground energy levels of the quantum dots. Assuming an initial indium composition, E_x^{g-g} and ΔE_g is calculated giving E_g^x . From this result of E_g^x the new indium content (x_{In}) and the new value for strain and ground states are calculated. This new strain and ground state transition energy lead to a new E_g^x . Iteration continues until indium content (x_{In}) converges.

The band gap of the InGaN is calculated from

$$E_g^x = x_{Ga}E_g^{GaN} + x_{In}E_x^{InN} - bx_{Ga}x_{In} \qquad (4)$$

where b = 2.77 / (1 + 1.007x_{In}) gives indium content dependent InGaN bowing parameter to match experimental data [69]. The effect of strain and piezoelectric effect on

bandgap at room temperature can be calculated by separating the effect of strain (ε) and piezoelectric fields (QCSE) as follows:

$$\Delta E_g = \Delta E_g^{\varepsilon} + \Delta E_g^{QCSE} \qquad (5)$$

As only the lowest possible transition in room temperature is of interest, the total change in band gap due to strain could be written as sum of the contributions from change in conduction and valance (heavy hole) bands, as in (6).

$$\Delta E_g^{\varepsilon} = \Delta E_c^{\varepsilon} - \Delta E_{v,hh}^{\varepsilon} \qquad (6)$$

For pseudomorphic wurtzite films grown along (0001) z-axis, the nonzero strain elements are [70]

$$\varepsilon_{xx} = \varepsilon_{yy} = \frac{c_{GaN} - c_{InGaN}}{c_{InGaN}} \qquad (7)$$

$$\varepsilon_{zz} = -\frac{2C_{13}}{C_{33}}\varepsilon_{xx} \qquad (8)$$

where c is the in-plane lattice constant and C_{ij} is the elastic constant.

The change in conduction band due to strain (ΔE_c^{ε}) is calculated [71], [72] as

$$\Delta E_c^{\varepsilon} = a_c^z \Delta\varepsilon_{zz} + a_c^{x,y}\left(\Delta\varepsilon_{xx} + \Delta\varepsilon_{yy}\right) \qquad (9)$$

$$= a_c^z\left(-\frac{2C_{13}}{C_{33}}\Delta\varepsilon_{xx}\right) + a_c^{x,y}\left(2\Delta\varepsilon_{xx}\right) \qquad (10)$$

where a_c^z and $a_c^{x,y}$ are hydrostatic deformation potential constants.

The calculation [70], [72] of valance band shift due to strain is as follows:

$$\Delta E^{\varepsilon}_{v,hh} = \lambda_{\varepsilon} + \theta_{\varepsilon} \quad (11)$$

$$\lambda_{\varepsilon} = D_1 \Delta\varepsilon_{zz} + D_2\left(\Delta\varepsilon_{xx} + \Delta\varepsilon_{yy}\right) \quad (12)$$

$$\theta_{\varepsilon} = D_3 \Delta\varepsilon_{zz} + D_4\left(\Delta\varepsilon_{xx} + \Delta\varepsilon_{yy}\right) \quad (13)$$

where D1, D2, D3, and D4 are deformation potential constants. By using Eqns. (6, 9, 11) the effect of strain on the band gap ($\Delta E^{\varepsilon}_{g}$) is calculated for any indium content in InGaN. Our result agrees that increasing the compressive strain ($\Delta\varepsilon_{xx}$ < 0) increases the band gap.

Polarization related electric field has two components: spontaneous and strain induced. Spontaneous component is independent of the strain and dependent on the composition. Strain induced one depends on composition via strain. Piezoelectric field is calculated from surface charge density. The surface charge density for both components can be calculated as [73], [74]:

$$\sigma^{z} = \sigma^{z}_{st} + \sigma^{z}_{sp} \quad (14)$$

$$\sigma^{z}_{st} = 2\varepsilon_{xx}\left(\varepsilon_{31} - \varepsilon_{33}\frac{C_{13}}{C_{33}}\right) \quad (15)$$

$$\sigma^{z}_{sp} = x_{Ga} P^{sp}_{GaN} + x_{In} P^{sp}_{InN} \quad (16)$$

where is P^{sp}_{AN} the spontaneous polarization coefficient of binary compound AN.

Piezoelectric field (ε^{PE}) follows the charge density as:

$$\varepsilon^{PE} = \frac{\sigma^{z}}{2\varepsilon_0 \varepsilon_r} \quad (17)$$

where ε_0 and ε_r are the vacuum and relative permittivity constants. Thus change in the band gap due to electric field, quantum-confined Stark effect (QCSE), could be approximated as [75]:

$$\Delta E^{QCSE}_{g} = \frac{C_1 (m^*_e + m^*_h) m_0 e^2 \varepsilon^2 L^4_{eff}}{\hbar^2} \quad (18)$$

where $C_1 = -2.19 \times 10^{-3}$ and $L_{eff} = 8 \times 10^{-10}$ m are used. m_0 is the electron mass, e is the unit charge, and ħ is the Planck's constant over 2π. m_e and m_h are the effective masses of the electron and heavy hole, respectively. L_{eff} is the effective thickness, and assumed to be the biggest QD height not to underestimate the change in the band gap due to electric field (ΔE^{QCSE}_{g}). ε is the electric field due to spontaneous and strain-induced charges. From (18), decreasing the electric field results in a larger band gap, as expected.

By using (10, 11, 18) in (19)

$$\Delta E_g = \left(\Delta E^{\varepsilon}_{c} - \Delta E^{\varepsilon}_{v,hh}\right) + \Delta E^{QCSE}_{g} \quad (19)$$

and iterating, indium content is determined to be 67.4% resulting a strain of -6.3%. The minus sign of strain indicates compressive nature. Due to small height of QDs, change in band gap due to electric field (~3.3 MV/cm) is on the order of -2.0 meV whereas change in band gap due to strain is 78.4 meV. The signs indicate the opposing processes. Thus, in QDs the effect of strain on band gap is dominant rather than that of piezoelectric fields. From FEM simulations, the converged ground energy levels of 0.217 eV for conduction band and 0.158 eV for valance band (measured from their respective bands) are reached as for $In_{0.67}Ga_{0.33}N$ QDs.

In quantum-well-based nitride light emitters, the emission blue shifts with increasing injection current due to free carrier screening that occurs due to the high piezoelectric field [31], [76]. This injection-dependent wavelength shift is undesirable for lasers as the gain structure is typically optimized for a single wavelength. Thus, QDs band gap being less affected by electric field should help more wavelength stable emission in nitride light emitters. As InGaN is sensitive to regrowth of GaN at high temperatures, these QDs could be particularly beneficial in hybrid structures [15] that employs ZnO layers grown atop of InGaN QDs at lower temperatures than that of (In)GaN layers.

E. Conclusion

Stranski–Krastanow growth of InGaN quantum dots (QDs) on GaN templates are realized. Effect of growth temperature, deposition thickness and V/III ratio on QD formation are studied. InGaN QDs with a peak emission wavelength of 558 nm at room temperature are realized. These QDs are capped to be integrated into optoelectronic devices. Theoretical analysis suggests that due to low QD height, piezoelectric field effect on band gap is small which should lead to more stable emission wavelength with injection current. InGaN QDs promises applications in conventional and hybrid green-light emitters.

VIII. Phosphor-free White Light-Emitting Diodes Based on InGaN Quantum Dots

High indium content (67%) room temperature green emitting InGaN quantum dots (QDs) are grown on GaN templates using Stranski-Krastanov (SK) growth mode. A two-step-grown GaN cap layer is employed for stacking QDs. Three-, seven- and fourteen-stack QD structures are integrated into light-emitting diodes from which cool white light emission is observed. The white light emission is attributed to the SK growth mode of InGaN QDs leading to blue and green emission from wetting layer and multi-stack QDs, respectively. Theoretical calculations identify compressive strain as the dominant effect on the emission characteristics of these QDs.

A. Introduction

Solid state lighting (SSL) holds the promise of a more energy-efficient, longer-lasting, more compact, and lower maintenance substitute for today's incandescent and uorescent light sources. Since lighting currently represents about 22% of all electricity consumption, the adoption of SSL could significantly reduce greenhouse gas emissions [11].

The development of high efficiency and reliable white

lighting is a crucial milestone for SSL research. One way to achieve white light is via mixing three-standard-color (red, green, and blue) light-emitting diodes (LEDs). This approach has the potential problems such as (1) the color of the light may change considerably with viewing angle, (2) color tuning individual diodes is difficult, (3) the operation life of different color LEDs are variable [77]. Development of high power blue LEDs [12], and lack of performance in green ones [13], [15] has led to another approach; the usage of a single (blue or ultraviolet) LED and one or more phosphors, as a means of white light generation [77]. Although recent phosphor-converted white LEDs show high efficiencies [78], phosphor-free white LEDs are more convenient in design, and more liable for mass production [79], [80].

With increasing indium content (from violet to green emission), a significant decrease in performance is observed in light emitters based on quantum wells [13]. One of the reasons is that the large lattice mismatch between high indium content InGaN and GaN induces the generation of dislocations in the active region [13], [57]. This explains how the performance decreases for high indium content light emitters, even on low dislocated templates [50], [58]. The use of quantum dots may be one way to overcome these limitations in high indium content devices. Besides, optoelectronic devices based on quantum dots (QDs) have many advantages over those based on quantum wells such as temperature stability and higher efficiency. [60]

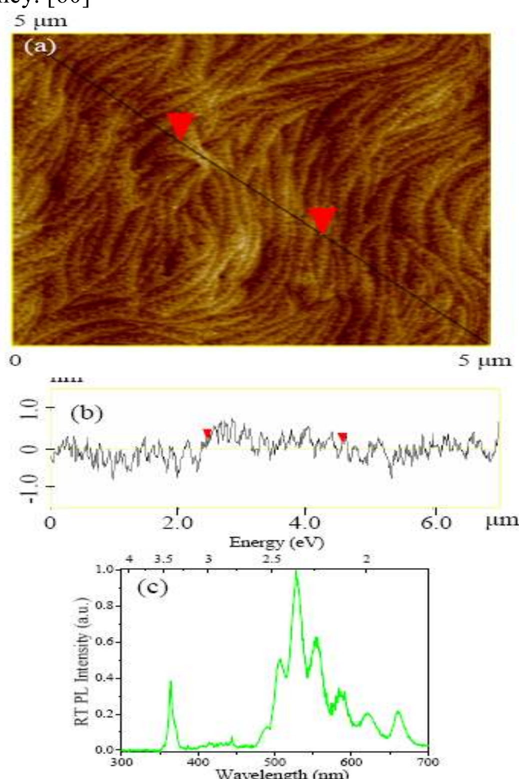

Fig. 53. (a)Atomic force microscopy (5 µm × 5 µm) contour images of InGaN on GaN after 6.5 ML InGaN, (b) Height variation across the cross section; The average quantum dot height is 0.8 nm (~3 ML), bottom diameter is 36 nm, and their density is 1×10^{10} cm^{-2} (c) Room temperature photoluminescence of the uncapped self-assembled QDs (Peak wavelength is 528.0 nm, and Full-width-at-half- maximum (FWHM) is 89.3 meV).

Room temperature blue emission from InGaN QDs has been reported earlier [61], [62]. The strong luminescence from these QDs is attributed to the exitonic transitions [63]. The blue QDs are being integrated into LEDs [64]. However, there are few reports of InGaN quantum dots in the green spectral range luminescing at room temperature [65]. This is mainly due to the difficulty in growing high indium content high quality InGaN quantum dots. The uniformity, density and size of the QDs are essential parameters controlled by material growth. Besides, successful integration of these QDs into LEDs requires their stability at high temperatures so that stacking could be realized and contact layers can be grown upon. In this respect, the instability of InGaN at high temperature adds another challenge for device applications [20]. However, the phase separation in InGaN can be suppressed by strain [81]. Thus, among high indium content InGaN active layers, InGaN QDs grown using Stranski-Krastanov (SK) growth mode [82] may be more phase-stable at higher temperatures than quantum wells as strain could be channelled for self-assembly rather than misfit dislocation generation. In this work, the structural and optical properties, and the capping of green emitting InGaN QDs grown via SK growth mode is studied. Integration of these QDs into LEDs is realized, and electro-optical characteristics of these LEDs are reported.

B. Experiment

InGaN QDs are self-assembled by SK growth on 2 µm GaN on double side polished (0001) sapphire (Al_2O_3) substrate using horizontal-fow low-pressure metal organic chemical vapor deposition (MOCVD) reactor. During the active layer growth, N_2 is used as the carrier gas to facilitate the incorporation of indium. InGaN deposition thickness is calculated based on bulk growth rate which was 1.2 nm /min at 100 mbar. In order to achieve high quality QDs, the deposition temperature from 734ºC to 634ºC , V/III ratio from 9×10^3 to 15×10^3 , deposition thickness from 2 ML to 8 ML (1 ML ≈ 2.7Å), interruption time from 15 s to 60 s are varied. Eventually, the growth temperature of ~634ºC, V/III ratio of ~13.9×10^3, deposition thickness of 6.5 ML and interruption time of 15 s were determined to give well-ordered InGaN QDs emitting in green regime at room temperature.

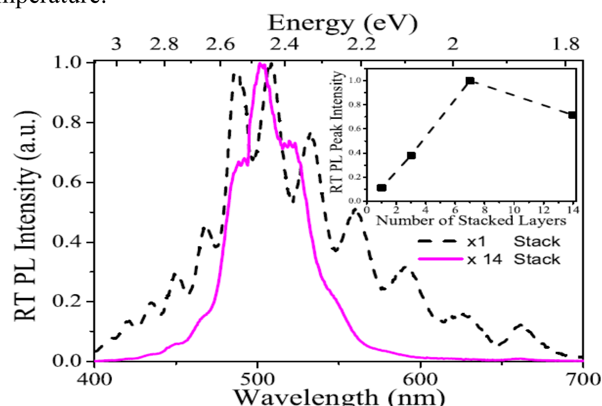

Fig. 54. Room temperature normalized photoluminescence intensity of a single- and fourteen-stack QD layer. Inset displays the relative PL intensity dependence on the number of stacked QD layers.

C. Result and Discussion

1) Growth and Characterization of InGaN QDs

No QD formation for layers thinner than critical thickness of 4.0 ML suggests the SK growth mode [68], [82]. After deposition of 6.5 ML and 15 s growth interruption under ammonia, quantum dots form (Fig. 53). The average size of the quantum dots are 0.8 nm (~3 ML) in height and 36 nm in bottom diameter, and their density is 1×10^{10} cm^{-2}, as seen in Fig. 53(a-b). It is observed in Fig. 53(a) that the QDs form at the step edges of the epitaxial layer as step edges increase the nucleation probability.

The photoluminescence of the InGaN QDs is studied at room temperature (Fig. 53 (c) and Fig. 54). Fig. 53(c) displays the room temperature luminescence from these uncapped QDs. The GaN energy level is observed at 364 nm as well as strong green luminescence related to high indium content InGaN QDs peaking at 528 nm. Fabry-Perot reflections (in Fig. 53(c) and 2) are observed due to 2 µm thick GaN cavity. Due to low excitation (18 W/cm^2), the main transition in QDs is from ground levels of conduction and valance bands. The emission band (400-450 nm) attributed to a wetting layer is observed at photoluminescence studies. The existence of this wetting layer is due to SK growth mode verified by AFM studies. The detrimental effect of quantum dot height on radiative lifetime is reported [66]. The strong room temperature luminescence of our QDs should be due to smaller QD height leading to a higher overlap between electron and hole wavefunctions, and higher QD uniformity and density leading to stronger luminescence. In conclusion, the critical thickness is determined to be 4.0 ML, and QDs with room temperature green emission is achieved by MOCVD growth optimization.

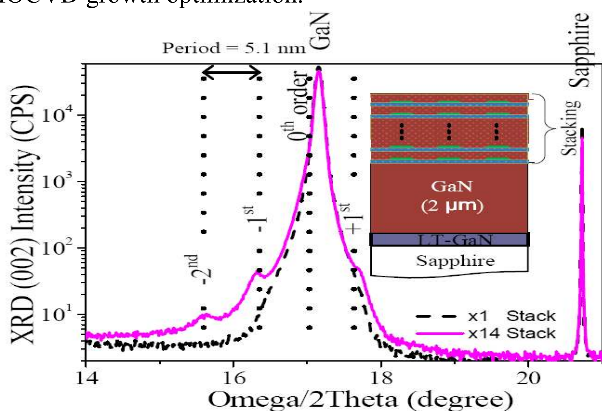

Fig. 55. Room temperature XRD (002) intensity of a single-and fourteen-stack QD layer. Inset displays the stacked structure.

2) Capping and stacking InGaN QDs

Integrating the QDs in LEDs requires an appropriate means of capping. Besides, achieving strong emission necessiates embedding many QD layers that are similar in characteristics. QD preservation and QD multi-stacking requirements are fulfilled by developing a two step cap layer: 2 nm low temperature ((~634ºC)) GaN layer followed by 2 nm high temperature (~1020ºC) GaN layer. The low temperature cap layer increases the QDs stability and durability under high temperatures, and high temperature growth creates a high quality GaN epilayer (verified by AFM) for the next stack of QDs. By this scheme, up-to fourteen QD layers are stacked up. The slight blue shift of the peak wavelength (83 meV) before (Fig. 53(c)) and after (Fig. 54) capping is attributed to the interdiffusion of indium atoms. The photoluminescence (PL) of a single stack and fourteen-stack QD layer is compared in Fig. 54. The narrowing of the PL spectra suggests successful capping. The peak wavelength is 510 nm and is not affected significantly by number of stacked QD layers. The Fig. 54 inset displays the dependence of the PL peak intensity on the number of QD stack layers. The linear increase in intensity up to seven stacks shows our stacking quality. Slight decrease for the fourteen-stack QD layer could be due to slight degradation in material surface with respect to seven-stack QD layer.

The stacked active layers are studied by X-ray diffraction (XRD) for monitoring crystal quality. Although no InGaN peaks can be identified for a single stack, fourteen-stack QD layer displays clear satellite peaks, as seen in Fig. 55. The increase in clarity of the satellite peaks with increase in stacked layer confirms the quality of the stacked active layers. The indium composition of the individual layers (wetting layer and QDs) is difficult to determine by XRD as all layers are under high stress, and their thicknesses are relatively comparable. Thus, optical luminescence results are used to determine the indium content of the QDs as explained in Section III C. XRD data determines the active layer period as 5.1 nm, which is comparable to expected period 5.8 nm, considering SK growth formation of active layer material: 1.8 nm (6.5 ML) active layer material (wetting layer and QDs), and 4 nm GaN cap layer. In conclusion, AFM, photoluminescence and XRD results show proper GaN capping scheme for green emitting InGaN QDs as being first a low temperature (2 nm), then a high temperature (2 nm) cap layer. Successful stacking up to fourteen QD layers is achieved.

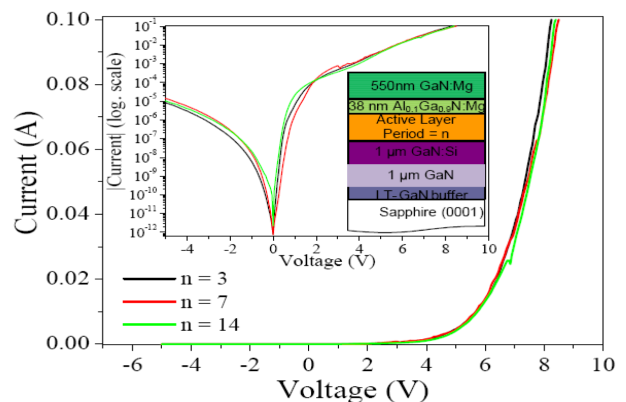

Fig. 56. I -V Curves of the LEDs for three-, seven-, and fourteen-stack QD layers. Inset displays the logarithmic scale I -V curves and the final LED device structure.

3) Integration of InGaN QDs into LEDs and Results

The integration of multi-stack QD layer in an LED is achieved by growing 38 nm thick $Al_{0.1}Ga_{0.9}N$:Mg as a current blocking layer, and followed by 550 nm GaN:Mg deposition as current spreading and contact layer. Complete device structure is shown in Fig. 56 inset.

Activation of the p-type GaN is achieved by rapid thermal annealing at 1000ºC for 30 s. After surface treatment with

$HCl:H_2O(1:1)$, 30Å Ni / 30Å Au is deposited as transparent contact and is annealed to achieve ohmic contact to p-type material. ECR-RIE system (etchants being $SiCl_2$ and Ar) is used to etch the mesa. 400Å Ti / 1200Å Au is deposited as the thick contact metal for both n- and p-type GaN.

The I-V curves of the LEDs with three-, seven-, and fourteen-stack QD layer is shown in Fig. 56. No significant difference in the I-V characteristics of the LEDs with respect to number of QD stack in the active layer is observed. The electrical equivalent values are calculated. [52] The on-series resistance (Rs) is ~17.2 Ω. Parallel resistance, which is inversely related to leakage current, is calculated as ~5G Ω. The turn-on voltage is 6.1 V.

A typical electroluminescence (EL) of an LED is shown in Fig. 57. The ~380 nm peak is due to electron overflow into p-type material, and their subsequent recombination in (Al)GaN:Mg layers. The broad electroluminescence from blue to green regime is due to the superimposition of emission from wetting layer and QDs. The wetting layer emitting from 400 nm to 450 nm (observed in Fig. 53(c)) has a stronger effect in EL due to higher carrier injection and carrier overflow from the QDs. The green emission band from 480 nm to 530 nm is attributed to the embedded InGaN QDs which demonstrated strong room temperature PL before integration into the LEDs (Fig. 54). Thus, LEDs employing self-assembled InGaN QDs are shown to be a good source of phosphor-free cool white light emission, that may be vital for SSL.

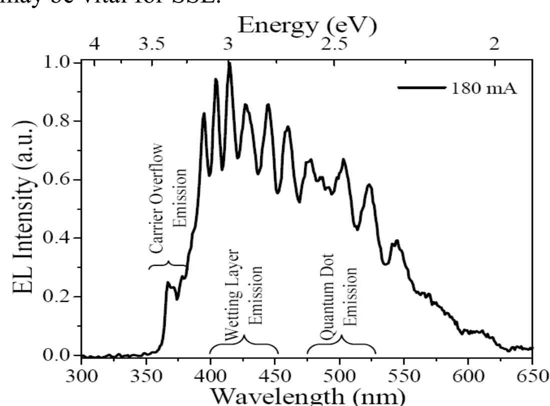

Fig. 57. A typical room temperature electroluminescence of the QD-based LED at 180 mA injection.

D. Conclusion

InGaN QDs are grown by SK growth mode and shown to have strong green luminescence at room temperature. A low temperature GaN cap layer followed by a high temperature one is developed for stacking up to fourteen-layer of QDs, which are later integrated into LEDs. Cool white light emission is observed from these LEDs that is applicable for SSL.

IX. Conclusion

A five-step LEO GaN growth technique for high quality LEO GaN growth is introduced. Blue and green emitting active layers and LEDs on conventional GaN and five-step-grown LEO GaN templates are realized. Significant differences in blue and green active layer surfaces are analyzed. The high quality LEO templates are observed to be important for smoother active layer surface morphologies. Blue and green LEDs on conventional GaN and high quality LEO GaN are studied. Green LEDs are observed to be leakier than blue ones, and no significant differences between green LEDs on conventional GaN and LEO GaN in terms of I-V behavior and peak power are observed. Green MQW quality is determined to be the bottleneck for high performance green emitters, not template dislocation density.

The green active layer quality is improved by using pulsed atomic layer epitaxy for InGaN. Thermal cycling in the active layer is developed to ensure uniformity and quality of the quantum wells. We have demonstrated green LEDs with emission wavelength 510 nm at 20 mA. A blue shift with injection current similar to blue LEDs are observed.

Employment of ZnO atop of green emitting high indium content InGaN LEDs brings up a new era of designs as it solves a major problem of conventional green LEDs: it prevents the much-needed indium for green emission from leaking out. Low indium incorporation in QWs grown on nonpolar substrates raises the interest in semipolar structures which promise higher rate of indium incorporation and significantly decreased piezoelectric fields. Combined with the semipolar freestanding GaN substrate, our innovative ZnO – InGaN hybridization promises efficiency-droop-free green LEDs with superior green spectral quality that fulfills the green gap and enables white LEDs based on color-mixing (the most energy efficient method of white light generation) as well as other commercial applications such as portable hand-held projectors/communicators, TVs and novel display systems.

Green emitting InGaN QDs are realized, and integrated into LEDs. Thanks to the S-K growth mode, white light emission is observed. These quantum structures could be of interest to phosphor-free lighting technologies.

In summary, III-Nitrides are quite promising materials from ultraviolet towards visible emitters. Their direct bandgap and its tunibility make them great candidates for portable energy efficiency alternatives whereas their durability and radiation hardness make them longer life time solutions for harsh environments. From quantum structures (such as dots) to bulk material systems, AlGaInN compounds promise a very bright future for the world.

Acknowledgment

The authors would like to thank Dr. J.L. Pau, Dr. R. McClintock, Dr. P. Kung, Dr. K. Minder, Dr. S.R. Darvish, Dr. S. Slivken and Dr. B. Movaghar from Center for Quantum Devices at Northwestern University for their support and feedback throughout the research.

References

[1] J.D. Brown, Jizhong Li, P. Srinivasan, J. Mathews, J. F. Schetzina, *MRS Internet J. of Nitride Semicond. Res*. **5**, 9 (2000).
[2] A. Yasan, R. McClintock, K. Mayes, S. R. Darvish, P. Kung, and M. Razeghi, *Appl. Phys. Lett*. **81**, 801 (2002).
[3] K. Mayes, A. Yasan, R. McClintock, D. Shiell, S. R. Darvish, P. Kung, and M. Razeghi, *Appl. Phys. Lett*. **84**, 1046 (2004).

[4] A. Yasan, R. McClintock, K. Mayes, D. Shiell, L. Gautero, S. R. Darvish, P. Kung, and M. Razeghi, *Appl. Phys. Lett*. **83**, 4701 (2003).

[5] D. J. Rogers, F. Hosseini Teherani, A. Yasan, K. Minder, P. Kung, and M. Razeghi, *Appl. Phys. Lett* 88, 141918 (2006).

[6] D. J. Rogers, F. Hosseini Teherani, A. Yasan, R. McClintock, K. Mayes, S. R. Darvish, P. Kung, M. Razeghi and G. Garry, *Proc. SPIE*, **5732**, 412 (2005).

[7] J. Fryar, E. McGlynn, M. O. Henry, A. A. Cafolla, C. J. Hanson, *Physica B*, **340-342**, 210 (2003).

[8] J. Lee, K. K. Kim, H. Tampo, A. Yamada, and S. Niki, *Journal of the Electrochemical Society*, **153**, G1047 (2006).

[9] X. Shao, S. L. Rommel, B. A. Orner, J. Kolodzey, and P. R. Berger, *IEEE Electron Device Letters*, **18**, 411 (1997).

[10] J.L. Pau, J. Piqueras, D.J. Rogers, F. Hosseini Teherani, K. Minder, R. McClintock, and M. Razeghi, *Journal of Applied Physics* **107**, 033719 (2010).

[11] C. J. Humphreys, MRS Bulletin 33, **459** (2008).

[12] N.F. Gardner, G.O. Muller, Y.C. Shen, G. Chen, S. Watanabe, W. Gotz, and M.R. Krames, *Appl. Phys. Lett.* **91**, 243506 (2007).

[13] Y.H. Cho, S.K. Lee, H.S. Kwack, J.Y. Kim, K.S. Lim, H.M. Kim, T.W. Kang, S.N. Lee, M.S. Seon, O.H. Nam, and Y.J. Park, *Appl. Phys. Lett.* **83**, 2578 (2003).

[14] I.K. Park, M.K. Kwon, J.O. Kim, S.B. Seo, J.Y. Kim, J.H. Lim, S.J. Park, and Y.S. Kim, *Appl. Phys. Lett.* **91**, 133105 (2007).

[15] C. Bayram, F. H. Teherani, D. Rogers, and M. Razeghi, *Appl. Phys. Lett.* **93**, 081111 (2008).

[16] Y. Narukawa, Y. Kawakami, M. Funato, S. Fujita, and S. Nakamura, *Appl. Phys. Lett*. **70**, 981 (1996).

[17] M. Takeguchi, M.R. McCartney, and D. J. Smith, *Appl. Phys. Lett.* **84**, 2103 (2004).

[18] S. J. Rosner, E.C. Carr, M.J. Ludowise, G. Girolami, and H.I. Erikson, *Appl. Phys. Lett.* **70**, 420 (1996).

[19] S.F. Chichibu, H. Marchand, M.S. Minsky, S. Keller, P.T. Fini, J.P. Ibbetson, S.B. Fleischer, J.S. Speck, J.E. Bowers, E. Hu, U.K. Mishra, S.P. DenBaars, T. Deguchi, T. Sota, and S. Nakamura, *Appl. Phys. Lett.* **74**, 1460 (1999).

[20] I. Ho and G.B. Stringfellow, *Appl. Phys. Lett.* **69**, 2701 (1996).

[21] B. Van Daele, G. Van Tendeloo, K. Jacobs, I. Moerman, and M.R. Leys, *Appl. Phys. Lett.* **85**, 4379 (2004).

[22] C. Wetzel, T. Salagaj, T. Detchprohm, P. Li, and J.S. Nelson. *Appl. Phys. Lett.* **85**, 866 (2004).

[23] S. Nakamura, M. Senoh, N. Iwasa, and S. Nagahama, *Jpn. J. Appl. Phys.* **34,** L797-799 (1995).

[24] S.J. Chang, W.C. Lai, Y.K. Su, J.F. Chen, C.H. Liu, and U.H. Liaw, *IEEE J. on Select. Top. On Quant. Elect.* **8,** 278 (2002).

[25] Y.D. Qi, H. Liang, D. Wang, Z.D. Lu, W. Tang, and K.M. Lau, *Appl. Phys. Lett*. **86**, 101903 (2005).

[26] T. Mukai, K. Takekawa, and S. Nakamura, *Jpn. J. Appl. Phys.* **27** L839-L841 (1998).

[27] D.I. Florescu, V.M. Asnin, F.H. Pollak, A.M. Jones, J.C. Ramer, M.J. Schurman, and I. Ferguson, *Appl. Phys. Lett.* **77**, 1464 (2000).

[28] P. Kozodoy, J.P. Ibbetson, M. Marchand, P.T. Fini, S. Keller, J.S. Speck, S.P. Denbaars, and U.K. Mishra, *Appl. Phys. Lett.* **73**, 975 (1998).

[29] D.S. Li, H. Chen, H.B. Yu, H.Q. Jia, Q. Huang, and J.M. Zhou, *J. Appl. Phys.* **96**, 1111 (2004).

[30] S. Tomiya, T. Hino, S. Goto, M. Takeya, and M. Ikeda, *IEEE J Sel. Top. Quant. Elect.* **10**, 1277 Nov./Dec. (2004).

[31] C. Bayram, J. L. Pau, R. McClintock, and M. Razeghi, *Applied Physics B* **95**, 307 (2009).

[32] S. Tomiya, K. Funato, T. Asatsuma, T. Hino, S. Kijima,T. Asano, and M. Ikeda, *Appl. Phys. Lett. 77*, 636 (2000).

[33] A.E. Romanov, P. Fini, and J.S. Speck, *J. Appl. Phys.* **93**, 106 (2003).

[34] H. Marchand, J.P. Ibbetson, P.T. Fini, S. Keller, S.P. DenBaars, J.S. Speck, and U.K. Mishra, *J. Cryst. Growth* **195**, 328 (1998).

[35] D. Kapolnek, S. Keller, R. Vetury, R.D. Underwood, P. Kozodoy, S.P. Denbaars, U.K. Mishra, *Appl. Phys. Lett.* **71,** 1204 (1997).

[36] H. Marchand, X.H. Wu, J.P. Ibbetson, P.T. Fini, P. Kozodoy, S. Keller, J.S. Speck, S.P. Denbaars, and U.K. Mishra, *Appl. Phys. Lett.* **73,** 747 (1998).

[37] M. Takeya, K. Yanashima, T. Asano, T. Hino, S. Ikeda, K. Shibuya, S. Kijima, T. Tojuo, S. Ansai, S. Uchida, Y. Yabuki, T. Aoki, T. Asatsuma, M. Ozawa, T. Kobayashi, E.Morita, and M. Ikeda, *J. Cryst. Growth* **221**, 646 (2000).

[38] X. Xu, R.P. Vaudo, J. Flynn, and G.R. Brandes. J. Electron. Mater. **31**, 402 (2002).

[39] A. Sakai, H. Sunakawa, and A. Usui, *Appl. Phys. Lett.* **73** 481 (1998).

[40] P. Fini, H. Marchand, J.P. Ibbetson, S.P. Denbaars, U.K. Mishra, and J.S. Speck, *J. Cryst. Growth* **209**, 581 (2000).

[41] J.Z. Domagala, Z.R. Zytkiewicz, B. Beaumont, J. Kozlowski, R. Czernetzki, P. Prystawko, amd M. Leszczynski, *J. Cryst. Growth* **245**, 37 (2002).

[42] K. Hiramatsu, Y. Kawaguchi, M. Shimizu, N. Sawaki, T. Zheleva, R.F. Davis, H. Tsuda, W. Taki, N. Kuwano, and K. Oki, *MRS Internet J. Nitride Semicond. Res.* **2**, 6 (1997).

[43] M.S. Ferdous, X. Wang, M. N. Fairchild, and S.D. Hersee, *Appl. Phys. Lett.* **91**, 231107 (2007).

[44] D. V. Kuksenkov, H. Temkin, A. Osinsky, R. Gaska, and M.A Khan, *J. Appl. Phys.* **83**, 2142 (1998).

[45] D. V. Kuksenkov, H. Temkin, A. Osinsky, R. Gaska, and M.A Khan, *Appl. Phys. Lett.* **72**, 1365 (1998).

[46] J.W.P. Hsu, M.J. Manfra, D.V. Lang, S. Richter, S.N.G. Chu, A.M. Sergent, R.N. Kleiman, L.N. Pfeiffer, and R.J. Molnar, *Appl. Phys. Lett.* **78**, 1685 (2001).

[47] S.J. An, J.H. Chae, G.C. Yi, and G. H. Park, *Appl. Phys.Lett.* **92**, 121108 (2008).

[48] Ya.I. Aliyov, J.E. Van Nostrand, and D.C. Look, *Appl.Phys. Lett.* **83**, 2943 (2003).

[49] D.J. Rogers, F.H. Teherani, P. Kung, K. Minder, and M. Razeghi, *Superlattice Microst.* **42**, p. 322-326 (2007).

[50] C. Bayram, J. L. Pau, R. McClintock, and M. Razeghi, *Journal of Applied Physics*. **104,** 083512 (2008).

[51] M. Smith, G. D. Chen, J. Y. Lin, H. X. Jiang, A. Salvador, B.N. Sverdlov, A. Botchkarev, H. Morkoc, and B. Goldenberg, *Appl. Phys. Lett.* **68**, 1883 (1996).

[52] E. F. Schubert, *Light-Emitting Diodes*, (Cambridge, Cambridge University Press, 2003).

[53] S.M. Sze, *Physics of Semiconductor Devices*, 2nd ed. (Wiley, New York, 1981).

[54] T. Takeuchi, C. Wetzel, S. Yamaguchi, H. Sakai, H. Amano, and I. Akasaki, *Appl. Phys. Lett.* **73**, 1691 (1998).

[55] C. Bayram**,** F. H. Teherani, D. Rogers, and M. Razeghi, *Vacuum Science and Technology B* **27**, 1784 May/June 2009.

[56] C. Bayram and M. Razeghi, *Applied Physics A* **96**, 403 (2009).

[57] F.A. Ponce, S. Srinivasan, A. Bell, L. Geng, R. Liu, M. Stevens, J. Cai, H. Omiya, H. Marui, S. Tanaka, *Phys. Status Solidi* **240**, 273 (2003)

[58] T. Kozaki, H. Matsumura, Y. Sugimoto, S. Nagahama, T. Mukai, *Proc. SPIE* **6133**, 613306 (2006).

[59] D.J. Eaglesham, M. Cerullo, *Phys. Rev. Lett.* **64**, 1943 (1990)

[60] M. Petroff, A. Lorke, A. Imomoglu, *Phys. Today* **54**, 46 (2001)

[61] K. Tachibana, T. Someya, Y. Arakawa, *Appl. Phys. Lett.* **74**, 383 (1999).

[62] B. Damilano, N. Grandjean, S. Dalmasso, J. Massies, *Appl. Phys. Lett.* **75**, 3751 (1999).

[63] O. Moriwaki, T. Someya, K. Tachibana, S. Ishida, Y. Arakawa, *Appl. Phys. Lett.* **76**, 2361 (2000).

[64] Y.K. Su, S.J. Chang, L.W. Ji, C.S. Chang, L.W.Wu,W.C. Lai, T.H. Fang, K.T. Lam, *Semicond. Sci. Technol.* **19**, 389 (2004).

[65] S. Choi, J. Jang, S. Yi, J. Kim, W. Jung, *Proc. SPIE* **6479**, 64791F (2007).

[66] V. Ranjan, G. Allan, C. Priester, C. Delerue, *Phys. Rev. B* **68**, 115305 (2003).

[67] I. Vurgaftman, J.R. Meyer, L.R. Ram-Mohan, *Appl. Phys. Rev.* **89**, 5815 (2001).

[68] K.S. Kim, C.H. Hong,W.H. Lee, C.S. Kim, O.H. Cha, G.M. Yang, E.K. Suh, K.Y. Lim, H.J. Lee, H.K. Cho, J.Y. Lee, J.M. Seo, MRS Int. J. Nitride Semicond. Res. **5S1**, W11.74 (2000).

[69] M. Androulidaki, N.T. Pelekanos, K. Tsagaraki, E. Dimakis, E. Iliopoulos, A. Adikimenakis, E. Bellet-Amalric, D. Jalabert, A. Georgakilas, *Phys. Status Solidi* **6**, 1866 (2006)

[70] S.L. Chuang, C.S. Chang, *Phys. Rev. B* **54**, 2491 (1996)

[71] M. Grundmann, O. Stier, D. Bimberg, *Phys. Rev. B* **52**, 11969 (1995).

[72] C.G. Van de Walle, M.D. McCluskey, C.P. Master, L.T. Romano, N.M. Johnson, *Mat. Sci. Eng. B* **59**, 274 (1999)

[73] O. Ambacher, J. Majewski, C. Miskys, A. Link, M. Hermann, M. Eicjkhoff, M. Stutzmann, F. Bernardini, V. Fiorentini, V. Tilak, B. Schaff, L.F. Eastman, J. Phys. Condens. Matter **14**, 3399 (2002)

[74] V.A. Fonoberov, A.A. Balandin, *J. Appl. Phys.* **94**, 7178 (2003)

[75] S.L. Chuang, *Physics of Optoelectronic Devices* (Wiley, New York, 1995)

[76] S. Chichibu, T. Azuhata, T. Sota, S. Nakamura, *Appl. Phys. Lett.* **69**, 4188 (1996)

[77] Eric D. Jones. *Light Emitting Diodes for General Illumination* (OIDA, Washington, 2001).
[78] S.C. Allen, and A. J. Stecki, *Appl. Phys. Lett.* 92, 143309 (2008).
[79] C.-F. Huang, C.-H. Lu, T.-Y. Tang, J.-Jie Huang, and C.C. Yang, *Appl. Phys. Lett.* **90**, 151122 (2007).
[80] C. B. Soh, W. Liu, J. H. Teng, S. Y. Chow, S. S. Ang, and S. J. Chua *Appl. Phys. Lett.* **92**, 261909 (2008).
[81] S.Yu. Karpov. *MRS Internet J. Nitride Semicond. Res.* **3**, 16 (1998).
[82] R. A. Oliver, M. J. Kappers, C. J. Humphreys, and G. A. D. Briggs, *J. Appl. Phys.* **97**, 013707 (2005).